creative commons

COMMONS DEED

저작자표시-비영리-변경금지 2.0 대한민국

이용자는 아래의 조건을 따르는 경우에 한하여 자유롭게

- 이 저작물을 복제, 배포, 전송, 전시, 공연 및 방송할 수 있습니다.

다음과 같은 조건을 따라야 합니다:

저작자표시. 귀하는 원저작자를 표시하여야 합니다.

비영리. 귀하는 이 저작물을 영리 목적으로 이용할 수 없습니다.

변경금지. 귀하는 이 저작물을 개작, 변형 또는 가공할 수 없습니다.

- 귀하는, 이 저작물의 재이용이나 배포의 경우, 이 저작물에 적용된 이용허락조건을 명확하게 나타내어야 합니다.
- 저작권자로부터 별도의 허가를 받으면 이러한 조건들은 적용되지 않습니다.

저작권법에 따른 이용자의 권리는 위의 내용에 의하여 영향을 받지 않습니다.

이것은 이용허락규약(Legal Code)을 이해하기 쉽게 요약한 것입니다.

Disclaimer

dCollection

工學博士學位論文

Fabrication of polypyrrole-based two-dimensional hybrid nanomaterials and their supercapacitor applications

폴리피롤 기반 2차원 하이브리드 나노재료 제조 및 슈퍼 커패시터로의 응용

2020年 2月

서울大學校 大學院

化學生物工學部

金 倫 基

Fabrication of polypyrrole-based two-dimensional hybrid nanomaterials and their supercapacitor applications

폴리피롤 기반 2차원 하이브리드 나노재료 제조 및 슈퍼 커패시터로의 응용

指導教授 張 正 植

이 論文을 工學博士 學位論文으로 提出함

2019 年 11 月

서울大學校 大學院

化學生物工學部

金 倫 基

金倫基의 工學博士 學位論文을 認准함

2019 年 11 月

委 員 長 ______________________ (印)

副委員長 ______________________ (印)

委 員 ______________________ (印)

委 員 ______________________ (印)

委 員 ______________________ (印)

Fabrication of polypyrrole-based two-dimensional hybrid nanomaterials and their supercapacitor applications

by

Yun Ki Kim

Submitted to the Graduate School of Seoul National
University in Partial Fulfillment of the Requirements for
the Degree of Doctor of Philosophy

February, 2020

Thesis Adviser: Jyongsik Jang

Abstract

Among the numerous studies about fabrication and in-depth research of nanomaterials, which has attracted the attention of many researchers for decades, the manufacture of organic/inorganic hybrid nanomaterials is of great interest at the same time. This trend follows the demand of the Internet of Things (IoT) era for light-weight energy storage devices using hybrid nanomaterials with both high performance and improved stability. The focus of this dissertation is on developing the functional hybrid materials by combining the advantages of both organic and inorganic materials and applying them to energy-storing electronic devices.

Two-dimensional (2D) nanomaterials have drawn a lot of attention since the groundbreaking discovery of single-layer graphene sheets over a decade ago. Thereafter, many 2D inorganic materials have been discovered and studied, and the carbonaceous materials such as organic molecules, carbon nanotubes, and polyolefins have been utilized to develop hybrid materials. There is a drawback in that the electrochemical behaviors of the resultant hybrid nanomaterials are mostly suppressed.

Conducting polymer (CP), accordingly, is a splendid candidate to retain the electrochemical properties, while enhancing mechanical and thermal stability when assembled as hybrid nanomaterials. As one of the most studied CPs, polypyrrole (PPY) has been scrutinized in view of high electrical conductivity, redox-active properties, and environmental stability. Nevertheless, a construction of PPY-based hybrid nanomaterials with 2D nano-bricks still remains a challenge.

This dissertation elucidates three different ways for fabricating PPY-based hybrids based on “integrative chemistry,” a method for material design where initial blocks are assembled *via* structuring reactions. MoS_2 nanosheet, phosphorene, and dopamine-coated CVD-grown graphene are used as building units, assembled with pyrrole monomers during the polymerization. In this research, three kinds of PPY-based hybrid nanomaterials fabricated by integrative chemistry were utilized as supercapacitor electrode materials, exhibiting improved performance as well as superior stability

Keywords: Hybrid nanomaterial; integrative chemistry; polypyrrole; MoS_2; phosphorene; graphene; supercapacitor

Student Number: 2014-22591

List of Abbreviations

AFM: atomic force microscopy

BP: black phosphorus

CP: conducting polymer

CV: cyclic voltammetry

CVD: chemical vapor deposition

DMF: dimethylformamide

DMSO: dimethyl sulfoxide

EDL: electrical double layer

EDLC: electrostatic double-layer capacitance

EIS: electrochemical impedance spectroscopy

ESS: energy-storage system

FE-SEM: field-emission scanning electron microscopy

FP: functionalized phosphorene

FPPY: functionalized phosphorene/polypyrrole

FT-IR: Fourier-transform infrared

GCD: galvanostatic charge-discharge

HOMO: the highest occupied molecular orbital

IHP: inner Helmholtz plane

IoT: Internet of Things

LPE: liquid-phase exfoliation

LUMO: the lowest unoccupied molecular orbital

MPY: MoS_2/polypyrrole

NMP: N-methyl-2-pyrrolidone

OHP: outer Helmholtz plane

PANI: polyaniline

PEDOT: poly(3,4-ethylenedioxythiophene)

PEN: polyethylene naphthalate

PPP: poly(*p*-phenylene)

PPY: polypyrrole

PT: polythiophene

PVA: poly(vinyl alcohol)

RP: red phosphorus

TEM: transmission electron microscopy

TMDC: transition-metal dichalcogenides

UV-Vis: ultraviolet-visible

VDP: vapor deposition polymerization

XPS: X-ray photoelectron spectroscopy

2D: two-dimensional

List of Figures

Table of Contents

2. Experimental Details..39

1. Introduction

1.1 Background

1.1.1. Conducting polymer

Conducting polymers (CPs) are plastics that are intrinsically electrically conductive based on their π-conjugated structures, hence are suitable candidates for systems which are required with metallic conductivity [1–3]. Many reports about CPs have been started since the first discovery that chemical treatment with iodine converts electrically insulating polyacetylene into a highly conductive material with electrical conductivity above 10^4 S cm^{-1}. Various types of CPs have been investigating a lot of interests, including polyaniline (PANI), poly(3,4-ethylenedioxythiophene) (PEDOT), poly(*p*-phenylene) (PPP), polypyrrole (PPY), and polythiophene (PT) as represented in **Figure 1**, and their derivatives.

The major feature which makes the CPs very auspicious is that they possess both electronic properties of semiconductors and polymeric properties such as low density, flexibility, and processibility [4–6]. In addition, CPs rapidly gain great attraction in new applications with increasingly processible materials with greater characteristics, high redox activity, and lower costs. In fact, using CPs over other materials has an advantage that the CPs are permeable to electroactive species, sufficiently conductive for current flow, easy to coat on various substrates, and easily modified. Accordingly, a tremendous amount of research has been carried out in the field of antistatic coating materials, field-effect transistors, sensors, flexible transparent displays, organic light-emitting diodes, electromagnetic shielding materials, actuators, electrochromic devices, printing electronic circuits, or corrosion-protecting materials, as depicted in **Figure 2** [7,8]. Especially, in view of electrochemical properties, CPs are also called synthetic metals. They can be applied as active materials for energy-storage devices as well on account of rapid doping/dedoping process with high charge density [9,10].

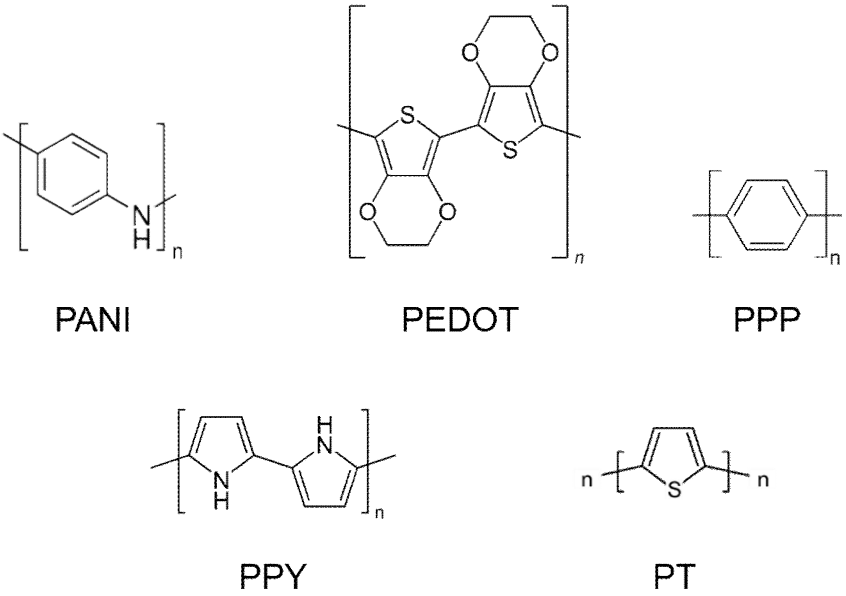

Figure 1. Molecular structures of representative conducting polymers.

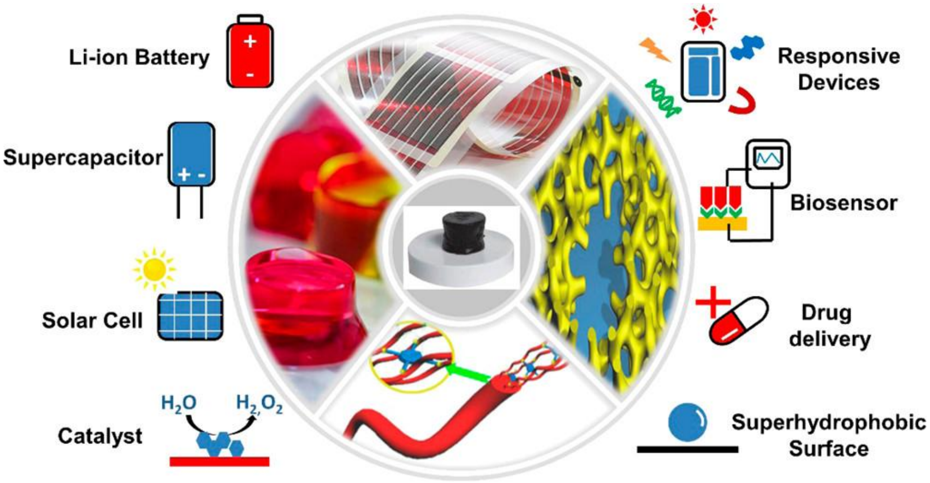

Figure 2. Applications of conducting polymers [7].

1.1.1.1. Polypyrrole

Polypyrrole (PPY), composed of five membered heterocyclic rings, has attracted considerable attention among the CPs because of its high electrical conductivity and good environmental stability [11–13]. The heteroaromatic and extended π-conjugated backbone structure of PPY provide it with chemical stability and remarkable electrical conductivity, respectively. PPY, hence, has been considered as one of the key materials to many potential applications such as electronic devices, electrodes for energy-storage systems, solid electrolytes for capacitors, electromagnetic shielding materials, and chemical sensors. Nevertheless, the π-conjugated backbone structure itself cannot satisfy appreciable conductivity. A chemical or an electrochemical process, referred to as doping, is imperative to achieve partial charge extraction from PPY chain [14,15]. This is a very worthwhile feature for applications where the electrical conductivity of a material must be controlled.

PPY, one of the most renowned CPs, is distinguished from other CPs that it can be easily p-doped, while being n-doped is very difficult because of the high positions of the highest occupied molecular orbital

(HOMO) and the lowest unoccupied molecular orbital (LUMO) levels [16].

Many conformational and structural defects can be formed during polymerization process. Conformational defects are α-α bondings with nonregular rotation and structural defects involve α-β bonds, hydroxyl groups, and carbonyl groups, where α-β coupling leads to branching and crosslinking and the oxygen-containing groups are introduced by the oxidations, as illustrated in **Figure 3**. These defects introduce structural disorders in the polymer chain, affecting the conjugation length and electrical conductivity [17,18]

Figure 4 describes the four different electronic band structures by the transition for doping level of the PPY chain. In the neutral state, PPY is an insulator with a large π-π* band gap of *ca.* 3.16 eV. However, when the PPY chain is doped with counterions to maintain electroneutrality during polymerization, a negative charge is extracted from the neutral segment of the chains. This gives rise to a local deformation from benzenoid to quinoid structure, forming a polaron. The formation of a polaron generates two localized electronic levels within the band gap (bonding/antibonding cation levels) while the unpaired electron occupies the bonding state. As the oxidative doping proceeds further, another electron is removed from the chain, resulting in the formation of a double-charged bipolaron. At higher oxidation level (exceeding *ca.* 33 %), the overlap between bipolarons is occurred, resulting in the formation of two narrow bipolaronic bands. This induces gradual diminution of band gap in terms of doping level, and **Figure 5** portrays resulting alteration of PPY in chemical structures.

PPY can be readily prepared by electrochemical and chemical approaches in both aqueous and non-aqueous solutions, as mentioned previously. Electrochemical preparation of PPY is not very intriguing for commercialization because of the difficulties in mass production and higher price compared to chemical preparation. It was deeply studied that PPY-halogen complexes prepared by chemical oxidative polymerization reveal relatively high stability at ambient temperature.

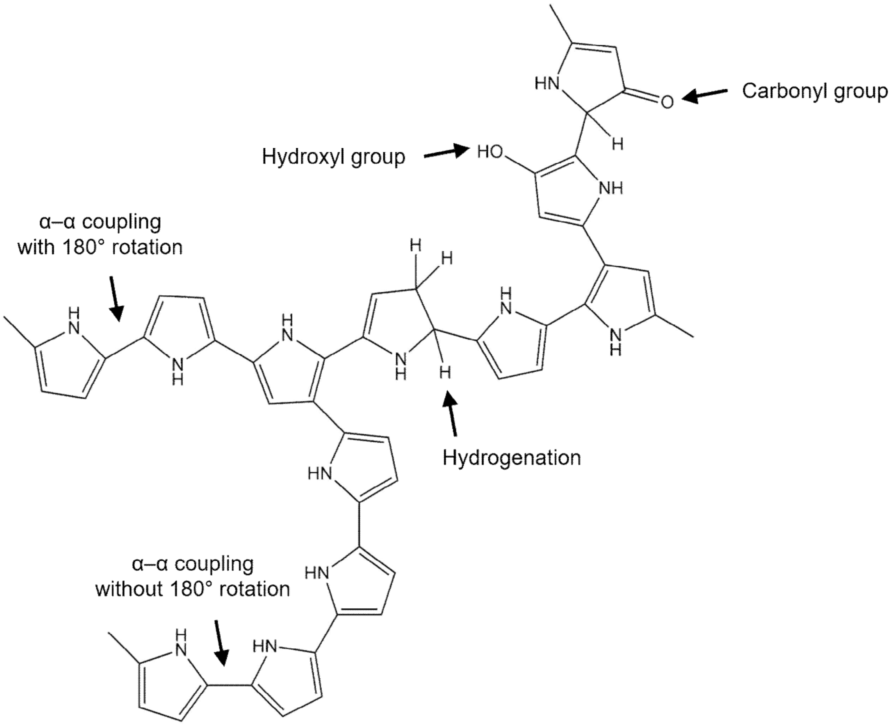

Figure 3. Possible chemical structures in polypyrrole chains.

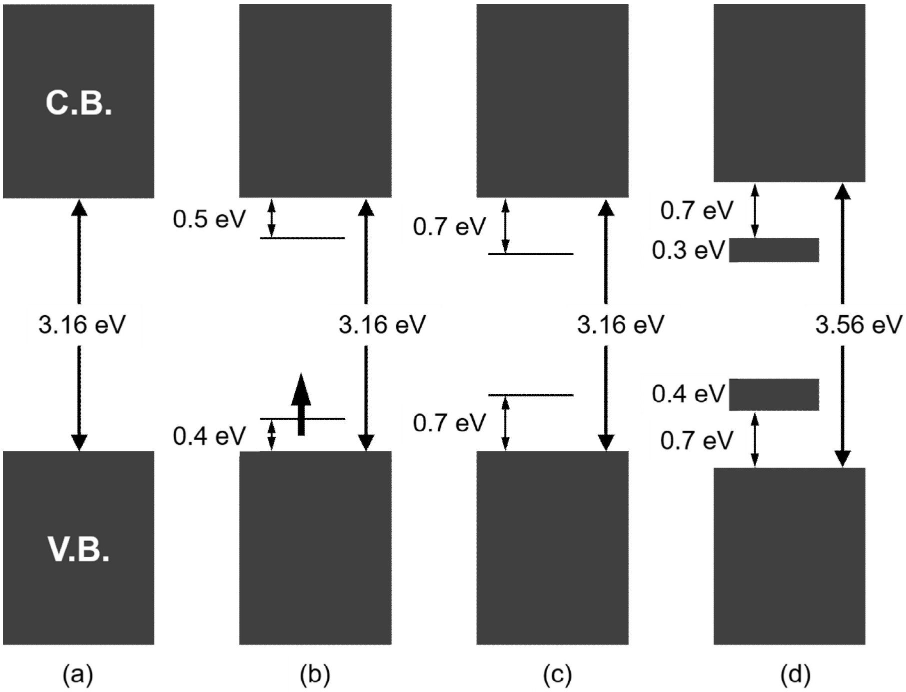

Figure 4. Electronic energy diagrams for (a) neutral, (b) polaron, (c) bipolaron, and (d) fully doped PPY.

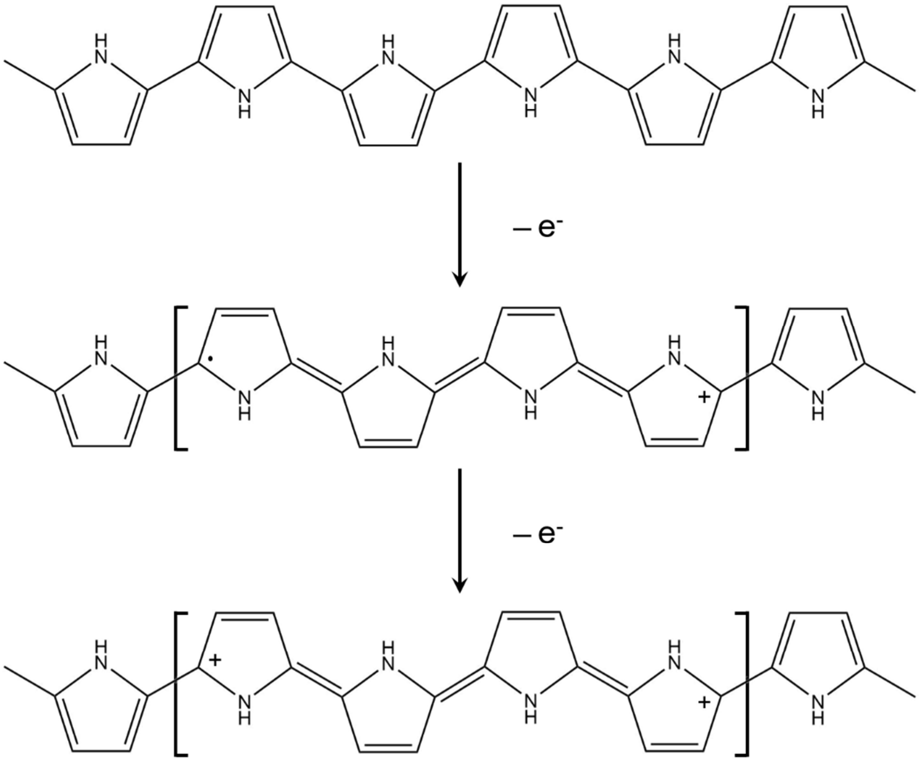

Figure 5. Chemical structures of (a) neutral, (b) polaron in partially doped, and (c) bipolaron in fully doped polypyrrole.

1.1.2. Two-dimensional nanomaterials

Among a great number of nanomaterials, two-dimensional (2D) nanomaterials are generally categorized either 2D allotropes of various elements or compounds (**Figure 6**) [19–21]. 2D nanomaterials have attracted substantial attention from researchers since Novoselov, Geim, and co-workers discovered graphene after exfoliation from graphite using mechanical cleavage method in 2004. Considered the thinnest materials, these are either single layers, or comprise of several layers with strong in-plane bonding and sheet-to-sheet van der Waals interactions. The electron confinement in two dimensions of 2D nanomaterials enables tailorable electronic properties compared to other nanomaterials, making them appealing candidates for fundamental study of condensed matter as well as electronic device applications such as fabricating inks, pastes, catalysts, sensors, gene delivery, and energy harvesting devices [22–26].

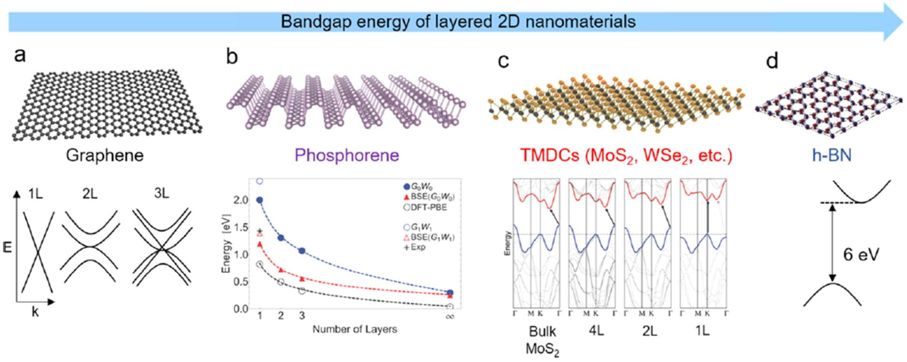

Figure 6. Lattice structures and layer-dependent band structures of layered 2D nanomaterials [20].

1.1.2.1. MoS_2 nanosheet

Molybdenum disulfide (MoS_2) is one of transition-metal dichalcogenides (TMDCs), and an analogous layered structure with graphene consisting of a Mo atomic layer sandwiched by two S atoms layers as illustrated in **Figure 7**. MoS_2 excels as a lubricant due to its layered structure as well as low coefficient of friction, dissipating energy by interlayer sliding when a shear stress is applied [27].

MoS_2 nanosheets have received great attention because of their distinctive features such as size-tunable catalytic, electronic, and optical properties. The presence of unsaturated d-orbitals as well as chemically active edge sites leads to be an attractive candidate for many potential applications such as catalysts, transistors, and electrode materials for energy-storage systems. Silimarly to other layered nanomaterials, MoS_2 exhibit band gap that can be differed from those in bulk [26–28]. As in **Figure 8**, the band gap changes from an indirect gap of 1.29 eV into a direct gap of 1.80 eV. In addition, MoS_2 with odd number of layers could produce oscillating piezoelectric outputs. Therefore, unique characteristics of MoS_2, *e.g.*, size-dependent band gap tuning and unique 2D geometry, high electrochemical activity, and chemical stability make it utilized in catalyst for hydrogen evolution, microelectronics, or photodetectors. MoS_2 nanosheet has attracted attention as a supercapacitor electrode material, still its low electrical conductivity limits its practical electrochemical performances despite a large number of advantages. Especially by hybridization with conductive carbon materials or phase transition to metallic phase, MoS_2 nanosheets can improve the electrochemical energy storage without the common restacking issues.

Liquid-phase exfoliation of 2D layered materials has become a widely used method to produce large quantity of 2D sheets from their parent bulk materials. 2D layered materials are constructed from a stacking of individual monolayers. Therefore, liquid-phase exfoliation requires the input energy enough to overcome the interlayer interactions. Accordingly, chemical or sonochemical exfoliation techniques of MoS_2 have been developed to produce the 2D nanosheets [29-31]. This process has developed to indulge the demand of nanosheet inks for printed electronic devices [32,33].

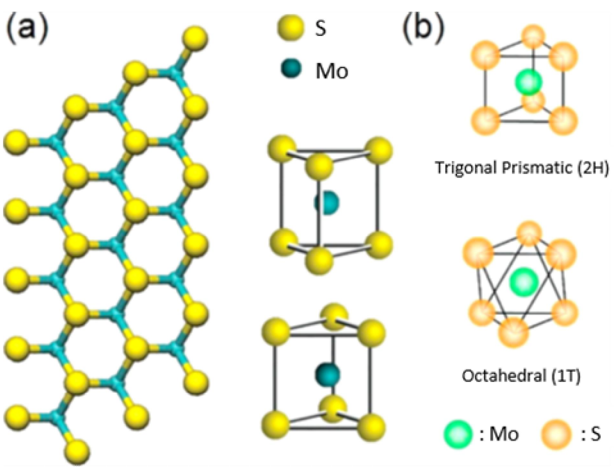

Figure 7. Crystal structure of MoS_2. (a) Top view of single layer hexagonal structure of MoS_2. (b) Trigonal prismatic (2H) and octahedral (1T) unit cell structures [27].

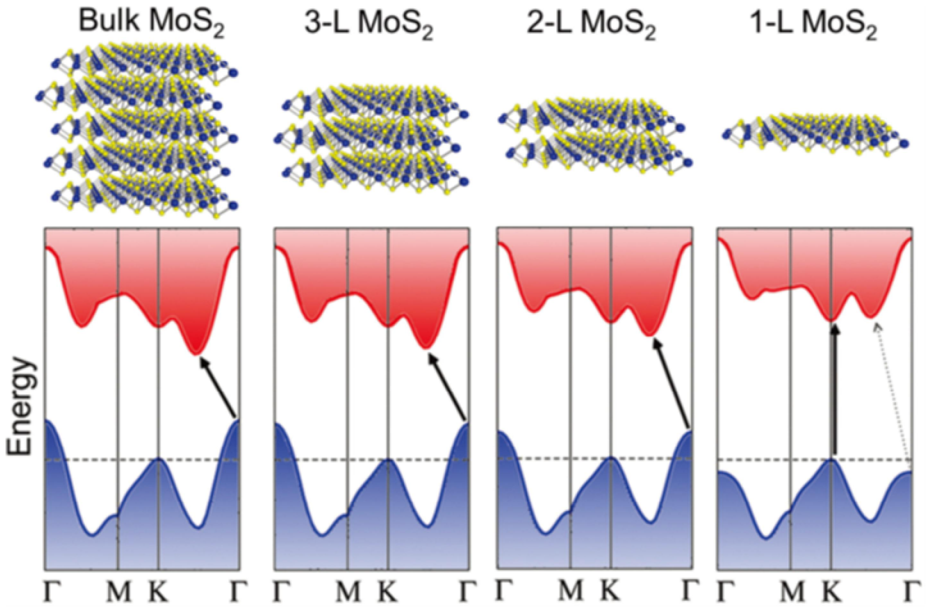

Figure 8. Thickness-dependent band gap of MoS$_2$ sheets. Bulk MoS$_2$ shows an indirect band gap of 1.29 eV, whereas in its monolayer form it has a direct band gap of 1.80 eV [28].

1.1.2.2. Phosphorene

Black phosphorus (BP), a layered three-dimensional crystal consisted of a stack of puckered layers of P atoms, as displayed in **Figure 9** [34]. BP has emerged as a next 2D nanomaterials recently, due to its exceptional characteristics. Among its characteristics, like other 2D nanomaterials, bulk BP has a direct band gap, and it changes its band gap depending on the number of layers, from 0.3 eV at bulk to 2.0 eV at single layer, as depicted in **Figure 10** [35,36]. Hence, BP has great potential applications such as light-emitting diodes, transistors, photodetectors, and photovoltaics.

Nevertheless, BP still has hindrance to be commercialized since the conditions to synthesize BP are very demanding. For example, red phosphorus (RP) is one of the phosphorus allotropes, and can be converted to BP at 8.5 GPa [37]. BP also can be prepared by vapor transport method using RP and SnI_2 at 500 ℃. Among the fabrication techniques, **Figure 11** displays high-energy ball milling technique that induces the temperature enough for phase transition of RP to BP. Accordingly, mechanical milling is a fascinating method to manufacture BP from RP in terms of mass production as well as cost savings [38,39].

The exfoliation energy of BP is found to be significantly greater than that of graphite, which accounts for the relative difficulty in exfoliating BP. Microcleavage of bulk BP using mechanical exfoliation ("scotch-tape" method), like the exfoliation of the graphene and TMDCs, can only produce small-size crystals. On the other hand, liquid-phase exfoliation (LPE), consisting of ultrasonic exfoliations of BP immersed into a solvent as shown in **Figure 12**, is suitable for large-scale production with a proper choice of solvent [40–43]. Furthermore, LPE can suppress the degradation of basal plane of phosphorene by choosing proper solvent like dimethylformaide (DMF), dimethyl sulfoxide (DMSO), and N-methyl-2-pyrrolidone (NMP). Still, its functionalization is necessary to utilize phosphorene as a building block of hybrid nanomaterials.

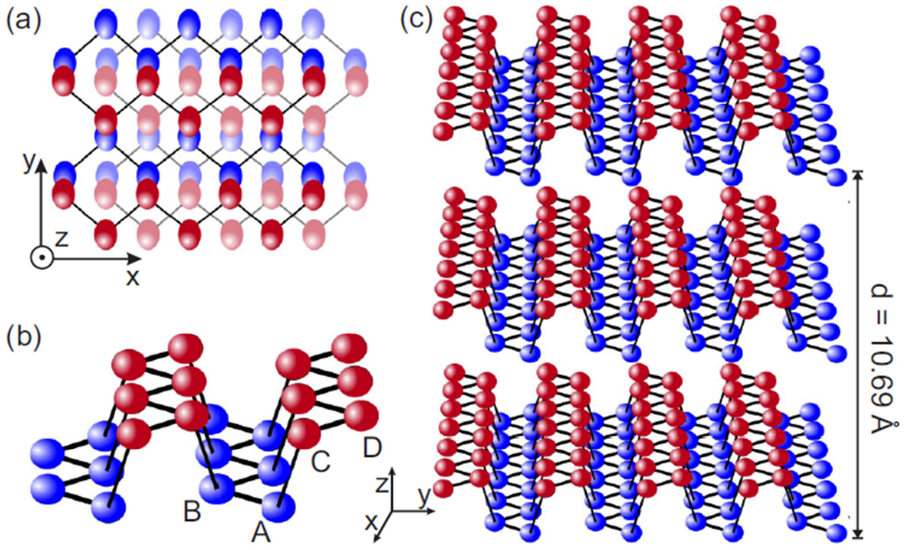

Figure 9. Schematic lattice structure of bulk BP, where P atoms at different sublayers are represented by different colors in each layer. (a) Top view of BP with AB stacking, and (b, c) side view of a single layer and N-layer BP, respectively [34].

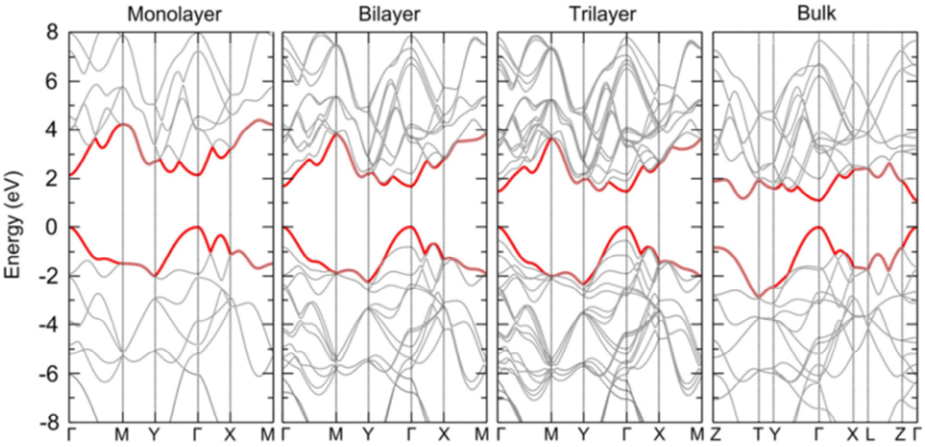

Figure 10. Calculated electronic band structure of monolayer, bilayer, trilayer, and bulk BP sheets at all high-symmetery points in the Brillouin zone [36].

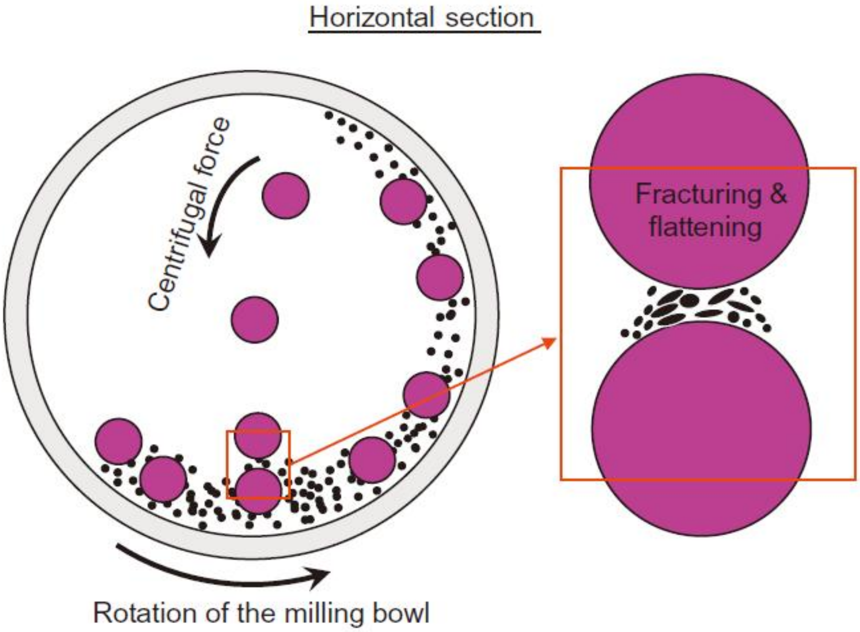

Figure 11. Schematic view of the motion of the ball and powder mixture [38].

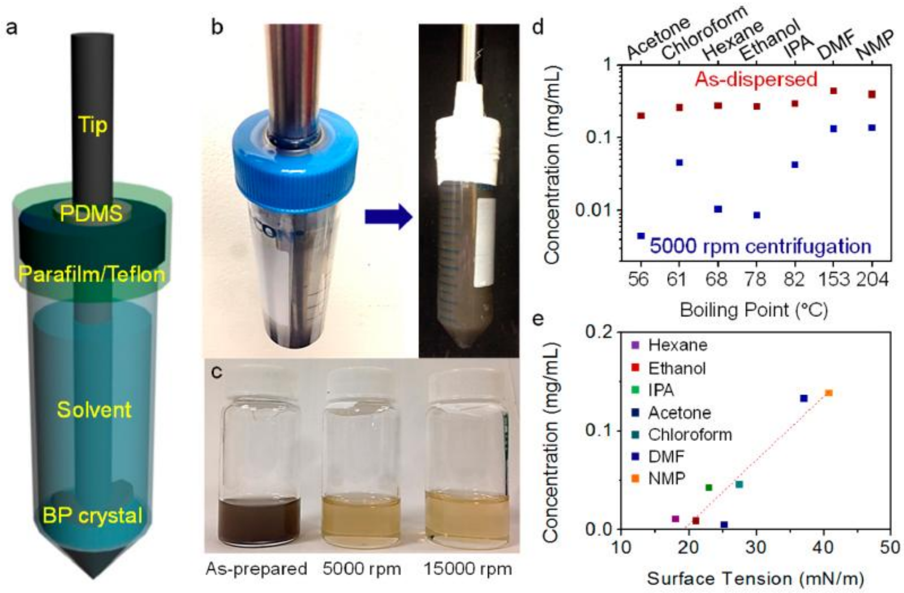

Figure 12. Liquid-phase exfoliation of BP in various solvents *via* tip sonication. (a) Schematic and (b) photograph of the setup to minimize air exposure during exfoliation. (c) Photograph of a BP dispersion in NMP after ultrasonication and centrifugations. (d, e) BP concentration plot for various solvents depending on the boiling point and surface tension, respectively [40].

1.1.2.3. Graphene

Graphene is a single atomic layer of sp^2 carbon atoms with a hexagonal honeycomb lattice as described in **Figure 13** [44]. As mentioned above, first discovery of few- and single-layer graphene nanosheets by mechanical exfoliation by bulk graphite powders began to draw attention to many researchers. Namely, graphene comprises of tightly packed carbon atoms with sp^2 orbital hybridization, and it has a theoretical specific surface area of 2630 $m^2\ g^{-1}$, a remarkable electron mobility of 15000 $cm^2\ V^{-1}\ s^{-1}$ at room temperature. A variety of exceptional properties such as unexpectedly high opacity and thermal conductivity, and the highest value of mechanical strength have led many to focus on graphene [45,46].

Figure 14 represents chemical vapor deposition (CVD), that it is one of the various methods that have been developed to produce large-scale graphene required for electronic device applications [47]. The large-scale production of graphene relies significantly on catalytic CVD. Ni and Cu (**Figure 14a** and **b**) are the most widely used catalysts due to their low cost, etchability and large grain size. In the case of Cu catalyst, the carbon intermediate is not dissolved in the Cu metal since the carbon solubility in Cu is negligible even at a very high temperature, thus surface adsorption of carbon precursors formulates graphene. Usage of Cu catalyst for CVD-grown graphene is suggested to be self-liniting that once the single layer of graphene is grown, the process does not propagate anymore because of the blockage of Cu surface. The CVD-grown graphene, as a result, shows off aforementioned properties.

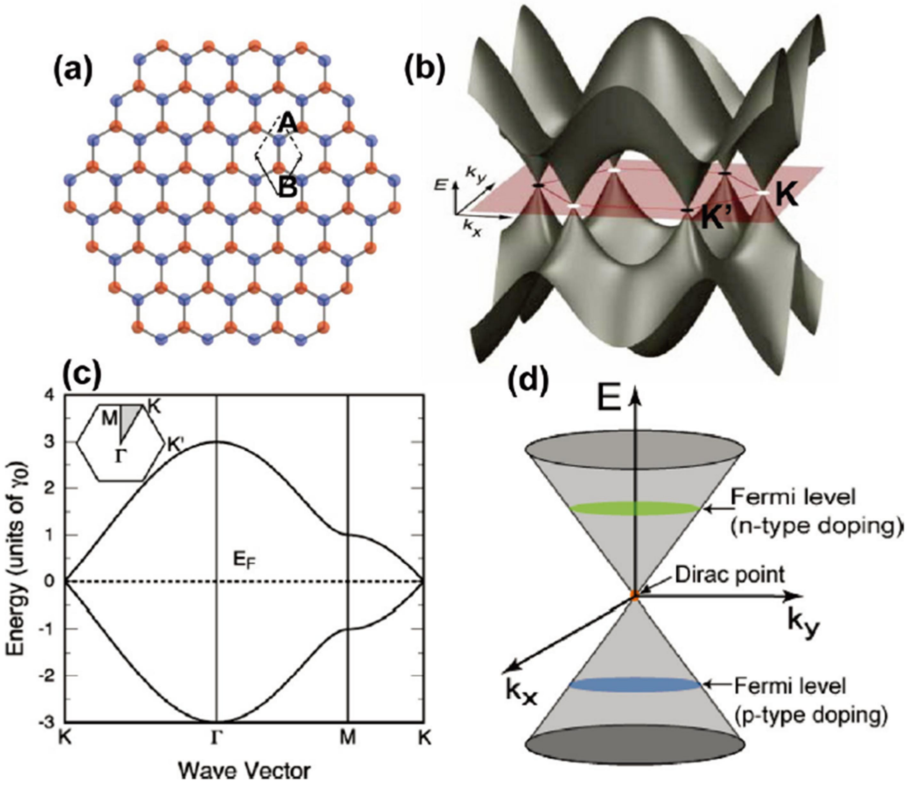

Figure 13. (a) Hexagonal honeycomb lattice of graphene with two atoms (A and B) per unit cell. (b, c) The 3D band structure and dispersion of the states of graphene. (d) Approximation of the low energy band structure as two cones contacting at the Dirac point [44].

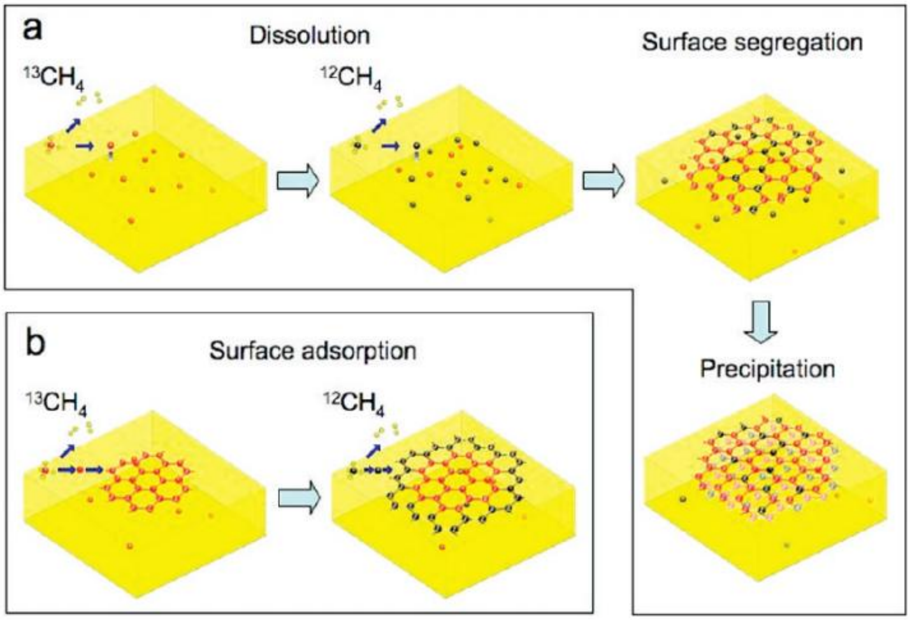

Figure 14. Schematic diagrams of the possible distribution of C isotopes in the graphene films based on growth mechanisms of (a) segregation and/or precipitation growth and (b) surface adsorption [47].

1.1.3. Hybrid nanomaterials

The demand for hybrid nanomaterials is exploding as they are considered potential platforms for applications in incredibly diverse fields e.g. micro-electronics, transportations, energy storage, diagnosis, housing, optics, environment, and Internet of Things (IoT) [48–50]. The combination of inorganic materials with polymeric compounds provides an excellent functionality with high performance as well as enhanced stability and good processibility. However, many of the well-established materials have their own limits to fulfill all technological desires in various applications. Recent approaches on the design of functional hybrid materials have been conducted a lot, still the expectations go beyond the properties of the estabilished materials. Therefore, many efforts have been devoted to synthesize novel functionalized hybrid nanomaterials for their specified potential applications.

1.1.3.1. Integrative chemistry

There are numerous bottom-up strategies for the fabrication of functional hybrid materials (**Figure 15**) [51–53]. One strategy to fabricate hybrid nanomaterials is based on the assembly of preformed monodispersed nano-objects. The objects can be preformed before the assembly, such as surface functionalization with ligands, spacers, organic molecules, etc. The prefabrication of the monodispersed components can be utilized as building blocks for hybrid materials. The nano-objects must be stable under the chemical conditions imposed during assembly. Accordingly, the components of the hybrid materials are linked by chemical bonds, allowing the development of well-defined structures that facilitate the performance of the final products [54,55].

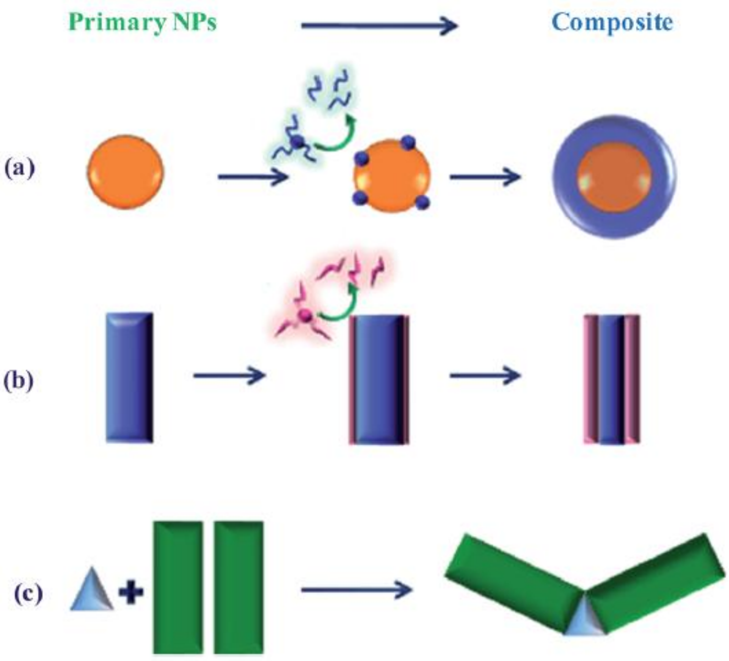

Figure 15. Schematic representation of bottom-up approaches to nanocomposites: (a) nanomaterials are decorated by a second material without altering their morphology; (b) nanomaterials are partially consumed by a chemical reaction, leading ultimately to the desired composite material, and (c) preformed nanomaterials are controllably aseembled like Lego building blocks [53].

1.1.3.2 Vapor deposition polymerization

Vapor deposition polyqmerization (VDP) has become the subject of attention across a variety of fields, from electronic parts to biocompatible materials [56,57]. Especially, a facile fabrication of hybrid nanomaterials by coating of polymers with various substrates is available through one-step VDP, as described in **Figure 16**. The VDP proceeds in a sequence of liquid monomer injection, decompression, and polymerization of monomer vapors. The resultant polymer layer can be uniformly coated onto the surface of the hard template materials.

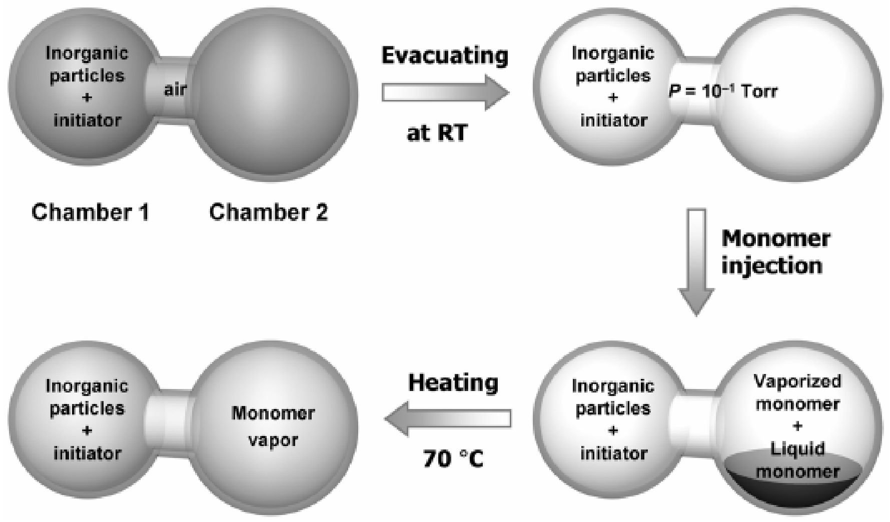

Figure 16. Schematic representation of the VDP for the encapsulation of the substrate materials [57].

1.1.4. Supercapacitor

Systems for electrochemical energy storage and conversion include batteries, fuel cells, and electrochemical capacitors [58]. These three systems have a common electrochemical base, although the storage and conversion mechanisms are different. Common features are that the energy-providing processes take place at the electrode/electrolyte interface and that electron and ion transport are separated. To compare the power and energy capabilities, a representative Ragone plot (**Figure 17**) discloses the relative positions of the energy-storing devices.

Among the so-called energy-storage system (ESS), electrochemical capacitor, or supercapacitor is used to describe a device that store an energy in the electrical double layer (EDL). As depicted in **Figure 18**, this EDL forms at the electrode/electrolyte interface with one layer at the surface inside the conductor and the other in the electrolyte almost instantaneously. When the charges are concentrated on each side of the electrode, the smaller ions are adsorbed, and the inner Helmholtz plane (IHP) refers to the distance of this closest approach of specifically adsorbed ions (genenrally anions). The distance of closet approach of nonspecifically adsorbed ions is referred to as the outer

Helmholtz plane (OHP), and these adsorption processes are determined by chemical affinities of the ions to the electrode and the field strength in the EDL. Unlike in batteries and fuel cells, the double layer at the electrode surface responds rapidly and the potential changes at the same time. When the physisorption/desorption process is only occurred, the device is called electric double-layer capacitor or electrostatic double-layer capacitor (EDLC). When the energy is mainly stored by a reversible faradaic charge transfer between electrolyte and electrode (pseudocapacitance), this type of capacitor is called pseudocapacitor [59].

Meanwhile, the innovative changes in the research and development of the electrochemical energy-storage devices lead to the proposal of several hybrid devices to satisfy the commercial views that have been formed on global warming and consumption of fossil fuels. Supercapattery, whose behavior is similar to that of supercapacitor with a greater energy capacity, is one of the proposed hybrid devices [60].

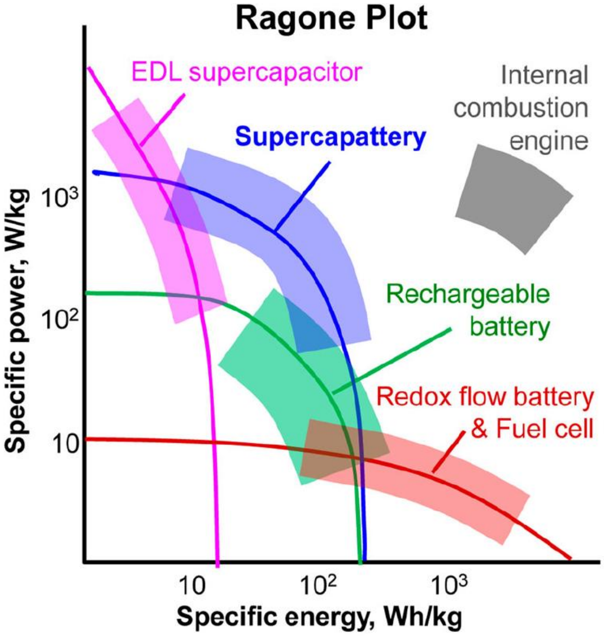

Figure 17. A relational position of supercapacitor and supercapattery to various energy technologies in Ragone plot [60].

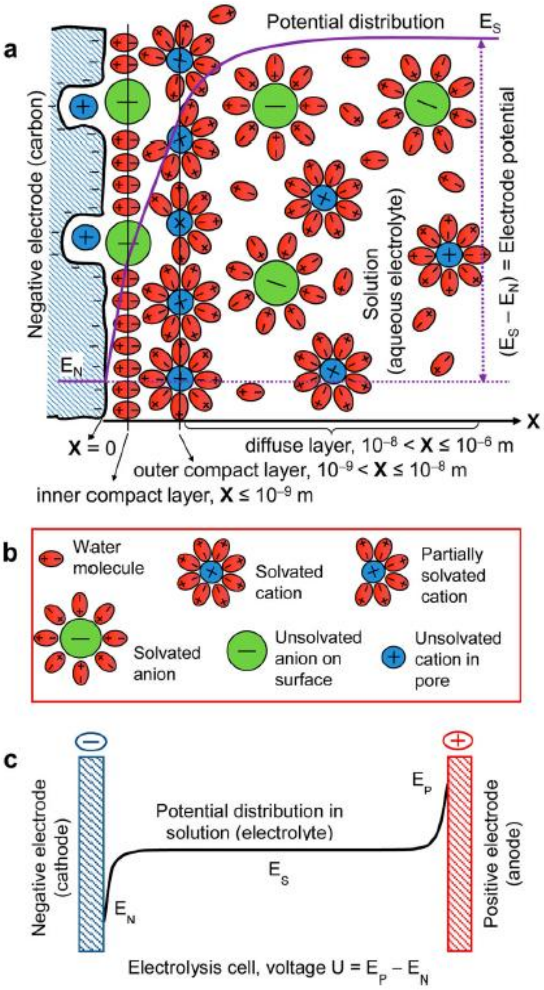

Figure 18. Schematic representation of (a) the EDL structure of the interface between an aqueous electrolyte and a porous electrode; (b) explanations of symbols in (a); (c) potential distribution in the electrolyte solution between the negative and positive electrodes in an electrolysis cell [59,60].

1.1.4.1. Flexible supercapacitor

Flexible energy-storage devices are attracting considerable attention due to the rapidly growing demand in portable, flexible, and wearable electronic devices [61]. Particularly, flexible supercapacitors require the electrode materials with additional characteristics like well-integrated mechanical flexibility. Thus, typical flexible supercapacitors are based on highly flexible thin-film electrodes with soft materials as substates.

Carbon-based materials such as graphene, carbon nanotube, and carbon cloth are strong candidates among the available materials, possessing the sufficient mechanical strength to endure various mechanical stresses and excellent electrical conductivity. Pure carbon materials have a low packing density, thus the capacitance of these carbonaceous materials is limited. Therefore, the introduction of conducting polymers or transition metal oxides/hydroxides with pseudocapacitance has been regarded as a solution to further strengthen the electrochemical performance. By creating a hybrid nanomaterial with the flexible substrate could be coupled with pseudocapacitive nanomaterials for higher electrochemical performance, while retaining the structural flexibility [62–64].

1.2. Objectives and Outlines

1.2.1. Objectives

In the precedent section, the significance of PPY-based 2D hybrid nanomaterials was introduced from the perspective on the practicability as well as academic research. The aim of this dissertation is to certify the fabrication method of PPY-based 2D hybrid nanomaterials with the prepared various 2D nanomaterials and to scrunitize their potentiality of supercapacitor. Particularly, 2D nanomaterials are fabricated by sonochemical exfoliation, phase transition and subsequent delamination, or CVD process, respectively. Hybridization with PPY is proceeded according to the fabrication method either utilizing molecular bricks to build the intended hybrid material, called “integrative chemistry”, or VDP method. Moreover, the electrochemical behaviors and supercapacitor performance of the PPY/2D hybrid nanomaterials are systemically investigated to identify the optimal conditions for the efficient supercapacitor electrode.

1.2.2. Outlines

This doctoral dissertation involves the following subtopics:

I. Fabrication of few-layer MoS_2 nanosheets and MoS_2/PPY hybrid nanocomposites by non-covalent bonding

II. Fabrication of functionalized phosphorene and FP/PPY hybrid nanocomposites by covalent bonding

III. CVD-grown graphene/PPY nanocomposites by introduction of interfacial layer

Each subtopics contains experimental details, characterizations of fabricated materials, electrochemical behaviors and supercapacitor performances.

2. Experimental Details

2.1. Few-layer MoS_2 nanosheets/PPY nanomaterials by non-covalent bonding

2.1.1. Materials

Molybdenum (IV) disulfide (MoS_2, powder, < 2 μm, 99 %), pyrrole (98%), and $FeCl_3$ (97%) were purchased from Aldrich Chemical Company and used without any purification. N-Methylpyrrolidone (NMP, 99.5%) and ethyl alcohol (99.5%) were purchased from Samchun chemicals.

2.1.2. Fabrication of few-layer MoS_2 nanosheets

Delamination of MoS_2 nanosheets from bulk MoS_2 was carried out by grinding and sonochemical exfoliation. Bulk MoS_2 powders (4.0 g, < 2 μm) were ground vigorously with NMP (4 mL) in a porcelain mortar for 30 min. Then, to remove all of the solvents, the mixture was placed in a vacuum oven. The dried powders were dispersed in a ethyl alcohol aqueous solution (45 vol%) by sonication for 2 h. After selecting the supernatants from the dispersion by leave the dispersion for 24 h, the dispersion was centrifuged to collect the MoS_2 nanosheet powders to utilize them for the fabrication of MoS_2/PPY hybrid nanomaterials.

2.1.3. Fabrication of few-layer MoS_2/PPY (MPY) hybrid nanomaterials

Few-layer MPY hybrid nanomaterials were prepared as follows. Pyrrole monomer was diluted ten-fold in DI water. As-prepared MoS_2 powders were put into a diluted aqueous solution of pyrrole monomer, which was then stirred for 2 h at the rate of 400 rpm. Pyrrole monomer was diluted in advance to improve the charge-charge interactions between MoS_2 and pyrrole molecules. The reaction was conducted at different temperature. A micropipette was used to add $FeCl_3$ aqueous solution (1 M), whose molar ratio of $FeCl_3$ to pyrrole was fixed as 1.75:1, and the resulting solution was mixed at 6000 rpm for 30 min. This solution was centrifuged at 10,000 rpm and 5 ℃ to remove the residual reagents from the resultants, and then repeated for three times with additional DI water. The final product was washed with ethyl alcohol and the precipitate was dried in a convection oven at 60 ℃ for 6 h.

2.1.4. Electrochemical measurement of MPY hybrid-based supercapacitor

To measure the electrochemical properties of the MoS_2/PPY nanomaterials, the materials were first dispersed in DI water at a concentration of 0.5 mg mL^{-1} by ultrasonication at 30% amplitude for 30 min. The prepared solution was drop-casted onto Au/PEN current collector. All the electrochemical measurements were conducted in H_2SO_4 aqueous solution (1 M) as an electrolyte. Three-electrode system was comprised of the prepared MoS_2/PPY electrode as a working electrode, Ag/AgCl in NaCl solution (3 M) as a reference electrode, and Pt wire as a counter electrode. Cyclic voltammetry (CV) was measured at a different scan rate in the range of 2 to 100 mV s^{-1}. Specific capacitance from the result of cyclic CV was calculated by following equation.

$$C = \frac{Q}{V} = \frac{\int I\,dt}{2mVv}$$

C: specific capacitance

Q: charge in Coulombs

V: potential window

$\int I\,dt$: integral of CV curve

m: mass of specimen

v: scan rate

In the case of galvanostat, the measurement was carried out with changing its specific current. The calculation of the specific capacitance from the result of galvanostatic charge-discharge curves was conducted by following equation,

$$C = \frac{Q}{V} = \frac{I}{mVt}$$

I: applied current

t: discharge time

where other parameters are the same as above. Electrochemical impedance spectroscopy was measured at potentiostatic condition whose voltage was fixed as 10 mV and the frequency in the range of 10^{7} to 10^{-2} Hz.

2.1.5. Characterization

Field-emission scanning electron microscopy (FE-SEM) images were collected using JSM-6701F (JEOL Ltd., Japan) installed at Seoul National University Chemical & Biological Engineering Research Facilities. Transmission electron microscopy (TEM) images and Raman spectra were acquired using JEM-2100 (JEOL) and Horiba Scientific T64000 spectrometer at the National Center for

Interuniversity Research Facilities (NCIRF) at Seoul National University. Topography of atomic force microscopy (AFM) was observed by a Digital Instrument Nanoscope IIIA (Veeco Instruments, Town of Oyster Bay, NY) in tapping mode with silicon tips (a resonant frequency of 320 kHz). X-ray photoelectron spectroscopy (XPS) spectra were obtained using Sigma probe (ThermoVG). Loresta-GP/MCP-T610 (Mitsubishi) was used to measure the electrical conductivity at ambient temperature by four-point probe method. Lambda 35 (PerkinElmer, Waltham, MA) UV-visible spectrometer was utilized to acquire the electronic behaviors of the materials. All the electrochemical characterizations were conducted by ZIVE SP2 electrochemical workstation (WonATech, South Korea).

2.2. Functionalized phosphorene/PPY nanomaterials by covalent bonding

2.2.1. Materials

Red phosphorus (RP, powder, > 98.0 %) was purchased from Yakuri Pure Chemicals and used without any purification. pyrrole (98%), pyrrole-3-carboxylic acid (≥ 96%), and $FeCl_3$ (97%) were obtained from Aldrich Chemical Company. Ethyl alcohol (99.5%) was purchased from Samchun chemicals.

2.2.2. Fabrication of phosphorene from red phosphorus

RP was phase transition of RP into black phosphorus (BP) by mechanical milling. RP powder (6 g) was put into a zirconia bowl with zirconia balls whose diameters are 1, 2, and 5 mm. The ball mill was conducted at 550 rpm and paused for 10 min for every 2 h, and a total duration of ball mill varied from 6 to 36 h. After milling, ethyl alcohol (30 mL) was poured into the bowl and it was milled at 400 rpm for 30 min. A mahogany-colored slurry was collected by micropipette, and was centrifuged to remove ethyl alcohol. This step fairly enhanced the yield of phase transition step approximately to 90%. The supernatant solution was removed and the precipitate was dried in a convection oven at 60 ℃ for 2 h. As-prepared BP powder was dispersed in ethyl alcohol solution (45 vol% in water) and sonicated for 2 h. The solvent was then removed by centrifugation and the phosphorene powder was collected by drying the precipitates at RT in a vacuum oven for overnight. Aqueous solutions for exfoliation of BP can also be used, but with the addition of stabilizing surfactants together with deoxygenated water to avoid exposure of phosphorene to oxidizing species, in general. This fabrication method is focused on the mass production of phosphorene, thus, a small portion of oxidized species is acceptable.

2.2.3. Functionalization of phosphorene

As-prepared phosphorene powder (0.6 g) and urea (1.2 g) was put into the zirconia bowls, and the ball mill was carried out at 600 rpm for 2 h. After ball mill, ethyl alcohol (30 mL) was again poured into the bowl, milling at 400 rpm for 30 min. The solvent was removed after centrifugation and the functionalized phosphorene (FP) was collected by drying in a vacuum oven for overnight. The FP has a low stability against humidity, thus the product was stored in a dessicator before usage.

2.2.4. Fabrication of functionalized phosphorene/PPY (FPPY) hybrid nanomaterials

The prepared FP powder was dispersed in DI water which a concentration of FP was 1.0 mg mL^{-1} by sonication for 1 h. Before fabricating the nanomaterials, pyrrole and pyrrole-3-carboxylic acid was mixed (molar ratio of 30:1) until pyrrole-3-carboxylic acid was dissolved thoroughly. This mixture was used as a monomer of carboxylated PPY. The mixture of monomer was put into the FP solution, stirring at RT for 2 h. An aqueous solution of $FeCl_3$ (1 M) was added with a fixed value of molar ratio of $FeCl_3$ to monomer of 1.75, and reacted for 1 h.

2.2.5. Electrochemical measurement of FPPY hybrid-based super-capacitor

The electrochemical properties of the FP/PPY nanomaterials were analyzed by both potentiostat and galvanostat. First, the materials were dispersed by tip-sonicator in DI water at a concentration of 0.5 mg mL^{-1}. The prepared dispersion was drop-casted onto Au/PEN current collector. All the electrochemical measurements were conducted in H_2SO_4 aqueous solution (1 M) as an electrolyte. Three-electrode system was comprised of the prepared hybrid nanomaterial electrode as a working electrode, Ag/AgCl in NaCl solution (3 M) as a reference electrode, and Pt wire as a counter electrode. Galvanostat as well as potentiostat were measured at a same condition of previous part mentioned before.

2.2.6. Characterization

Transmission electron microscopy (TEM) images and Raman spectra were obtained using a JEM-2100 (JEOL Ltd., Tokyo, Japan) and Horiba Scientific T64000 spectrometer at the National Center for Interuniversity Research Facilities (NCIRF) at Seoul National University, respectively. FT-IR spectra were collected with Frontier spectrophotometer (PerkinElmer). X-ray photoelectron spectroscopy (XPS) spectra were recorded using Sigma probe (ThermoVG). ZIVE SP2 electrochemical workstation (WonATech, South Korea) was used for all the electrochemical characterizations.

2.3. CVD-grown graphene/PPY hybrid nanomaterials by introduction of interfacial layer

2.3.1. Materials

Pyrrole (98%), $FeCl_3$ (97%), $CuCl_2$ (97%), dopamine hydrochloride (95%), and poly(vinyl alcohol) (PVA, average Mw 31,000–50,000) were purchased from Sigma-Aldrich Chemicals Company and used without any purification.

2.3.2. Chemical vapor deposition of graphene

Graphene was synthesized on polycrystalline copper foil by chemical vapor deposition (CVD) process. The copper foil was cut (8 cm × 8 cm) and was placed in the quartz-tube furnace. The temperature was increased to 1000 ℃ with a flow of H_2 (8 sccm) under 140 mTorr of pressure, and held for 30 min. CH_4 was introduced (20 sccm) for 20 min, and the furnace was cooled to room temperature. After the growth of the graphene, the other side of Cu foil was etched by atmospheric O_2 plasma to remove excess graphene. And by using a wet-transfer method, the prepared polycrystalline graphene was transferred onto the poly(ethylene 2,6-naphthalate) (PEN) film.

2.3.3. Fabrication of CVD-grown graphene/PPY (CDPY) hybrid nanomaterials by vapor deposition polymerization

Since the CVD-grown graphene barely has hydrophilic groups on the surface, the graphene was treated with atmospheric O_2 plasma before applying dopamine solutions. Then, the dopamine solution and one of the initiator solutions, either $FeCl_3$ (ferric chloride) or $CuCl_2$ (cupric chloride), fully covered the graphene after spin coating in sequence. Both the dopamine and the initiator salts are dissolved in DI water in advance. Although the concentration of the dopamine varies in the range of 0.2–2.0 mg mL^{-1}, that of the initiator solution is fixed as 1 M. In sequence, the film was placed into the glass apparatus to proceed vapor deposition polymerization. The gaseous pyrrole monomers were polymerized with previously applied initiators on the graphene, forming PPY layer under vacuum at RT, and the fabrication of either CDPY-Fe or CDPY-Cu, depending on the initiator, is completed. In the case of CPY-Fe or CPY-Cu, all the steps were conducted except for applying dopamine onto the CVD-grown graphene.

2.3.4. Electrochemical measurement of CDPY hybrid-based supercapacitor

High-resolution transmission electron microscopy (HR-TEM) and transmission electron microscopy (TEM) images were obtained using

A fabrication of all-solid-state full cell devices is conducted as follows. First, PVA powder was dissolved in the DI water (5 wt%) at 60 ℃, and the PVA solution was casted onto the quartz plate. The plate was heated at 60 ℃ for overnight to remove all of the solvent. The PVA film was easily detached from the quartz plate, and the film was soaked completely in the H_2SO_4 aqueous solution (1 M). The residual solution on the film was wiped, and the prepared PVA/H_2SO_4 solid electrolyte film was sandwiched by two equivalent electrodes of CDPY-Fe nanomaterial. The stack was slightly pressed during the electrochemical measurements.

2.3.5. Characterization

A JEOL 6700 instrument was used to obtain FE-SEM images. The topography of atomic force microscopy (AFM) was determined by a Digital Instrument Nanoscope IIIA (Veeco Instruments) in tapping mode using silicon tips with the resonant frequency of 320 kHz.

Raman spectroscopy was conducted by Horiba Scientific T64000 spectrometer at the National Center for Interuniversity Research Facilities (NCIRF) at Seoul National University. ZIVE SP2 electrochemical workstation (WonATech) was used for all the electrochemical measurement, including potentiostat, galvanostat, and impedance spectroscopy.

3. Results and Discussion

3.1. MPY hybrid nanomaterials by non-covalent bonding

3.1.1. Fabrication of few-layer MoS_2 nanosheets

Bulk MoS_2 powders are successfully exfoliated into few-layer MoS_2 nanosheets. New additional steps for selecting a certain size of MoS_2 nanosheets were carried out by centrifugation to acquire few-layer nanosheets, followed by precipitation and drying process to obtain MoS_2 nanosheets in a powder form. The additional steps resulted in size selection of the few-layer nanosheets as well as a high-yield production which is imperative for commercialization. The final yield of few-layer MoS_2 nanosheets was approximately 62.5% [65].

The size and the morphology of the as-prepared few-layer MoS_2 nanosheets were identified by TEM images in **Figure 19a**. It was confirmed the exfoliation of MoS_2 whose lateral size was in the range of 200–400 nm. The bulk MoS_2 powder was much larger, on the contrary, which the lateral size before the exfoliation was bigger than 1 μm. Moreover, AFM was utilized to determine the thickness and the lateral size of the nanosheets deeply. By analyzing the height profile in **Figure 19b**, the thickness of the MoS_2 nanosheets was measured as *ca.* 5.1 nm, representing that the exfoliated MoS_2 nanosheets consist of about five layers since the thickness of monolayer MoS_2 is close to 1 nm [66]

Raman spectroscopy was scrutinized to achieve structural understanding of the prepared few-layer MoS_2 nanosheets (**Figure 20**). Two prominent peaks at 380 and 406 cm^{-1} corresponds to the in-plane phonon mode E_{2g}^1 and out-of-plane phonon mode A_{1g} of MoS_2 nanosheets, respectively. Since the gap between two peaks becomes broader with more layers because of the stiffening of A_{1g} peak, the number of the layer can be determined from its gap. Given that the gap between E_{2g}^1 and A_{1g} was *ca.* 25.7 cm^{-1}, it can be estimated that the MoS_2 nanosheets are comprised of five layers, in accordance with the thickness measured by AFM [65,67].

UV−Vis spectroscopy was investigated at room temperature to understand the electronic behaviors of the prepared few-layer MoS_2 nanosheets (**Figure 21**). The resultant UV−vis spectrum provided information on the excitonic transitions in the MoS_2 nanosheets. Prior to measuring UV−vis spectroscopy, the MoS_2 nanosheets were suspended and diluted in a mixture of ethyl alcohol and DI water. Notable peaks were observed at 629 nm (1.97 eV) and 696 nm (1.78

eV), which suggest the existence of monolayer MoS_2 nanosheets. Two peaks verifies the direct transitions of A and B excitons at the K point of the Brillouin zone, respectively. Moreover, the shoulder peaks at 806 nm (1.54 eV) and 895 nm (1.39 eV) with small intensity correspond to the indirect-gap transitions of MoS_2 nanosheets. These results were in reasonable agreement with previous results [68,69].

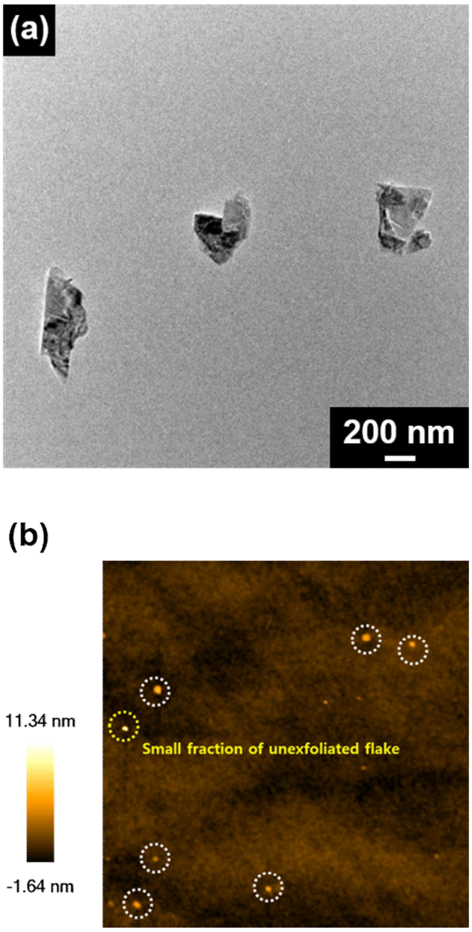

Figure 19. Topological analysis of the MoS_2 nanosheets. (a) TEM image shows the lateral size of the MoS_2 in the range of 200–400 nm, and (b) The average thickness by AFM is about 5.1 nm with small portion of unexfoliated flakes.

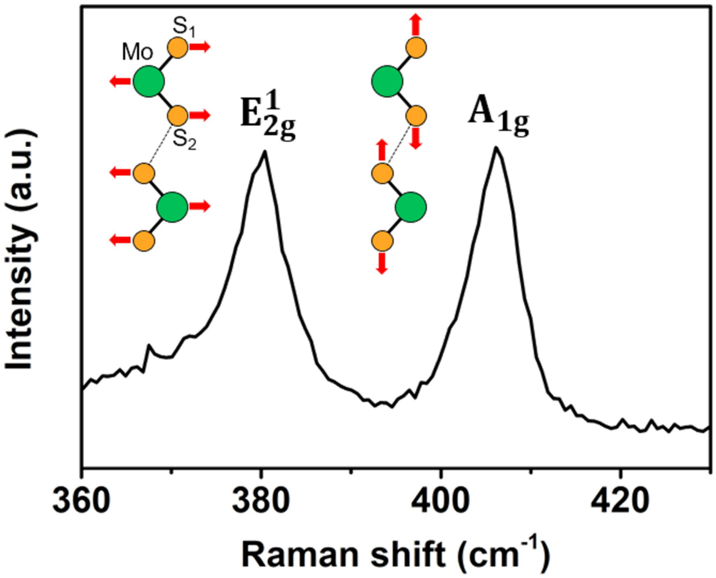

Figure 20. Raman spectrum of the MoS_2 nanosheets.

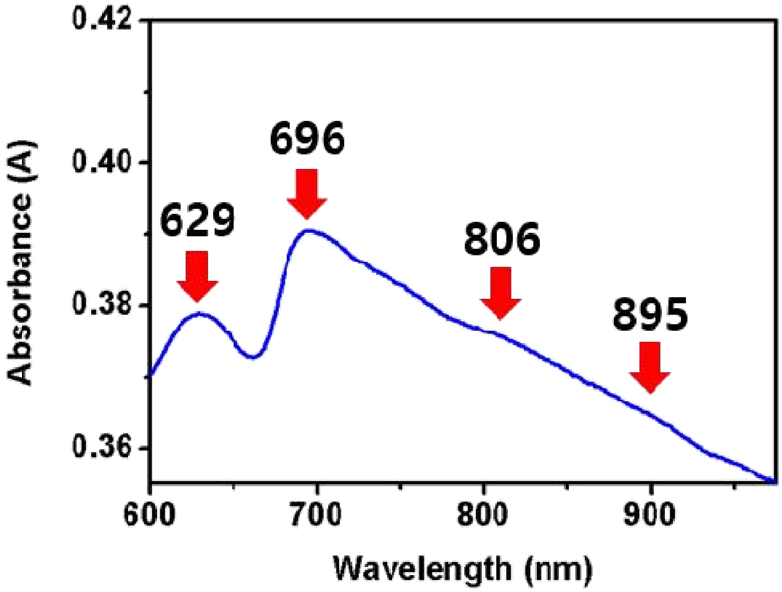

Figure 21. UV-visible spectrum of the MoS_2 nanosheets.

3.1.2. Fabrication of MPY nanomaterials

The MoS_2 nanosheets who work as 2D inorganic substrate of PPY, were dispersed and stirred with different ratio of pyrrole to MoS_2. A positive charge of pyrrole and a negative charge of MoS_2 cause them being held together by non-covalent bonding. $FeCl_3$ acts as an oxidizing agent for the polymerization of pyrrole, hence aqueous solution of $FeCl_3$ (1 M) was added. A molar ratio of $FeCl_3$ to pyrrole was fixed as 1.75:1 to maximize the electrical conductivity of PPY. The reaction was initiated as soon as the addition of $FeCl_3$ solution, changing its color to dark green.

TEM images in **Figure 22** are for the MoS_2/PPY (MPY) hybrid nanomaterials, representing their morphological changes as a function of the gravimetric ratio of pyrrole to MoS_2. The size, population and the morphology of decorated PPY is controlled. The materials of the hybrid MoS_2/PPY with their ratios of pyrrole to MoS_2 are 0.5, 1.0, 2.0, 5.0, and 10 are denoted as MPY_0.5, MPY_1.0, MPY_2.0, MPY_5.0, and MPY_10, respectively. As in the TEM images, the formation of PPY is diminutive in population for MPY_0.5, showing gradual increase with higher ratio of pyrrole, MPY_2.0 begins to represent a full coverage of PPY on MoS_2 nanosheets. Meanwhile, when it comes to the transition of its morphology, MPY_2.0 has PPY nanospheres grown on the surface of MoS_2 with their radii *ca.* 20 nm, respectively. Furthermore, PPY begins to change its morphology from sphere to rod for MPY_5.0. A higher ratio of pyrrole makes PPY accretes with MoS_2 nanosheets with higher aspect ratio of *ca.* 3.0. The morphology displays its transition again for MPY_10 that wad-like structure of PPY is formed.

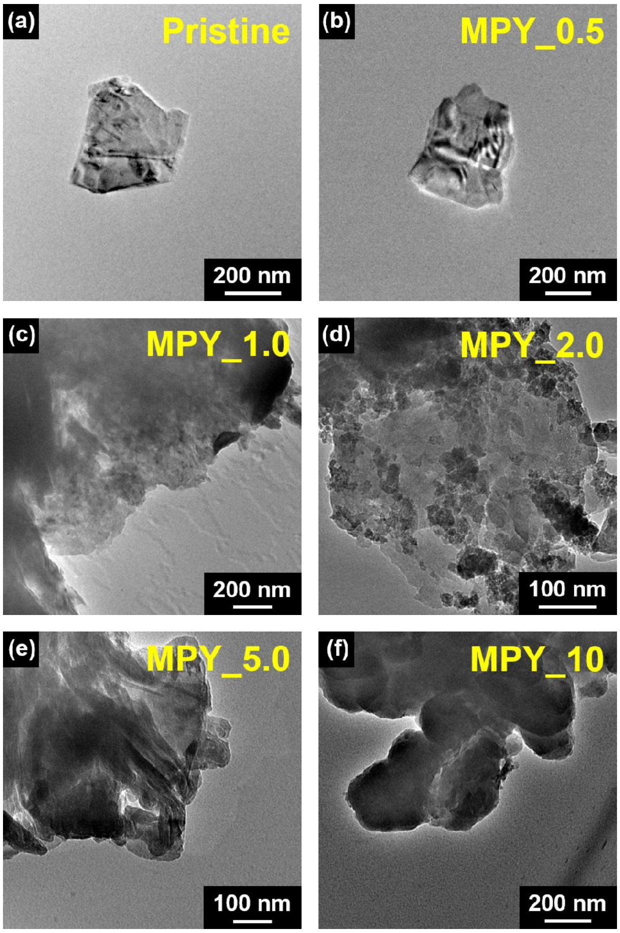

Figure 22. TEM images of the (a) MoS_2 nanosheet and (b–e) the MPY hybrid nanomaterials with the change of PY/MoS_2 ratio. (b) MPY_0.5, (c) MPY_1.0, (d) MPY_2.0, (e) MPY_5.0, and (f) MPY_10.

3.1.3. Material characterization of MPY hybrid nanomaterials

The structural information about the MoS_2/PPY hybrid nanomaterials was scrutinized by Raman spectroscopy using an excitation wavelength of 633 nm. All the samples were pelletized at a pressure of 7 metric ton for standardization. **Figure 23** indicates Raman spectra of the MPY hybrid nanomaterials as a function of the gravimetric ratio between pyrrole and MoS_2. Along with the TEM images representing PPY-decorated MoS_2, the characteristic peaks from MoS_2 as well as PPY were detected at the same time. To begin with, the PPY layer induced several peaks by its own bipolaron and polaron structures. The ring deformations attributed to bipolaron and polaron induced the peaks at 935, 984 cm^{-1}, respectively. The peaks at 1056, 1083 cm^{-1} are turned out to be C–H in-plane bending vibrations of reduction/oxidation states, respectively. The shoulder peak at 1257 cm^{-1} is from N–H in-plane deformation, and the peaks at 1369, 1414 cm^{-1} arise from C=C/C=N in-plane vibrations. In addition, C=C backbone stretching of reduction/oxidation states brought about the peaks at 1583, 1601 cm^{-1}, respectively [70].

Besides, the characteristic peaks of MoS_2 were observed simultaneously in the case of MPY_0.5 and MPY_1.0. Four major peaks correspond to in-plane phonon E_{2g}, out-of-plane phonon A_{1g}, an overtone of longitudinal acoustic phonons at the M point of the Brillouin zone (2LA(M)), and an asymmetric translations of both Mo and S atoms along *c*-axis noticed at 381, 405, 452, and 462 cm^{-1} [71]. The characteristic peaks of MoS_2 nanosheets were unnoticeable when the ratio of MoS_2 was lower, and this is due to a low population of PPY in the hybrid nanomaterials. In other words, when PY/MoS_2 of pyrrole to MoS_2 is 2.0 or greater, PPY not only grows on the surface of the MoS_2 nanosheets, but it fully covers the nanosheets, changing its morphology from nanosphere to nanorod to wad-like shape, as represented in TEM images.

X-ray photoelectron spectroscopy (XPS) was adopted to measure elemental composition and electronic state of the elements within the nanomaterials. **Figure 24** displays the XPS spectra of MoS_2/PPY nanomaterials that a deconvolution of the XPS spectra determines the fabrication of the materials. Three components are detected in C 1s region, which are C–C/C=C (284.5 eV), C–N (286.4 eV) bonds from PPY, and C–O (287.6 eV), C=O (288.6 eV) bonds by partial oxidation of PPY. In the case of N 1s region, four peaks were observed corresponding to PPY. The peaks at 398.0, 399.3, 400.4, and 401.9 eV, and are attributed to imine (–N=) group, amine (–NH–) group, positively charged nitrogen polaron ($–NH^+–$) and bipolaron ($=NH^+–$) of PPY, respectively [72,73]. In addition, it clarifies that the MoS_2 nanosheets are connected with PPY by Mo–N bonding (394.7 eV), being formed during the polymerization [74,75]. The presence of Mo–N bonds indicates that PPY layers have been formed on the surface of the MoS_2 nanosheets, and the interaction lowers its interfacial resistance between MoS_2 and PPY, which will be discussed below.

As one of the layered transition-metal dichalcogenides, MoS_2 has poor electrical conductivity to be utilized as a supercapacitor electrode material, otherwise it limits its practicality of the electrochemical performance. Hence, a reinforcement of the electrical conductivity is necessary for MoS_2 nanosheets. In especial, surface conductivity is one of the factors accurately affecting to supercapacitor performance. **Figure 25** represents the change of the surface conductivitiy of MPY hybrid nanomaterials as a function of the PY/MoS_2 ratio. Pristine MoS_2 nanosheet has its conductivity of 3.6×10^{-7} S sq., while the conductivity dramatically increases to 155 S sq. even when the PY/MoS_2 weight ratio is 0.5 (MPY_0.5), the minimum. The surface conductivity keeps rising as more monomers take part in the reaction.

It shows an increment to 378, 991 S sq. in the case of MPY_1.0 and MPY_2.0, respectively. This change is resulting from the population growth of PPY layers on MoS_2 nanosheets. The surface conductivity reveals its maximum value for MPY_2.0, which is due to population increment of the PPY nanospheres. As the PY/MoS_2 ratio increases, the surface conductivity began to decrease that the MPY_5.0 and MPY_10. PPY nanospheres become agglomerated, and as a result, the conductivity of MPY hybrid was 552 and 364 S sq., respectively. During the hybridization of PPY with MoS_2 nanosheets, the large difference of the conductivity may induce the chain morphology more linearly [76]. The linearity was at its maximum when PY/MoS_2 is 2.0, and the α-β couplings began to increase with higher PY/MoS_2 ratios.

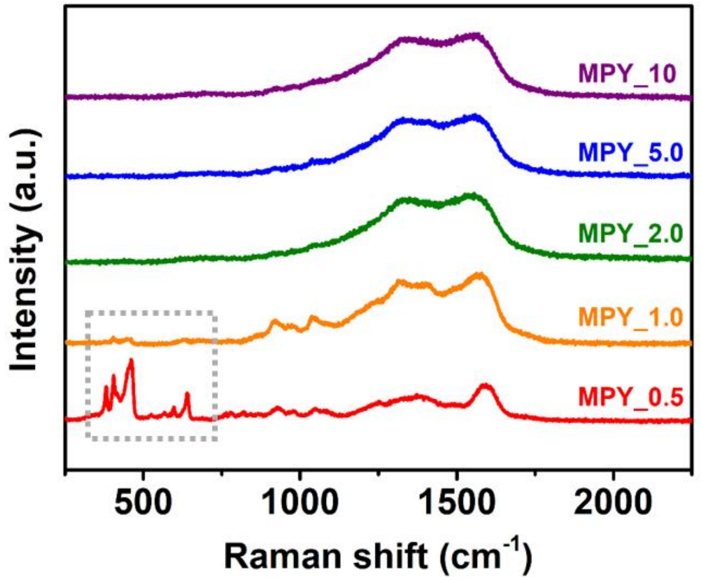

Figure 23. Raman spectra of MPY hybrid nanomaterials as a function of the PY/MoS$_2$ ratio from 0.5 to 10.

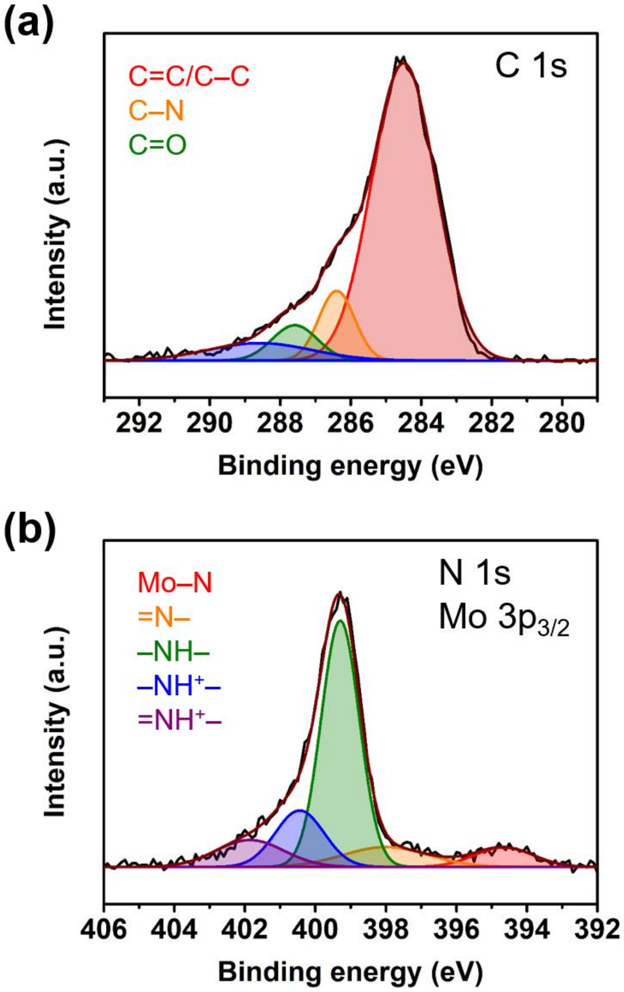

Figure 24. XPS spectra of (a) C 1s and (b) N 1s and Mo $3p_{3/2}$ of MPY_2.0.

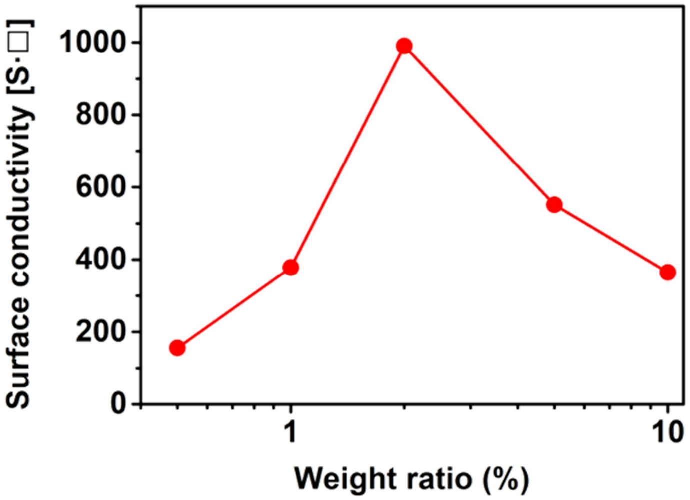

Figure 25. The change of surface conductivity of MPY hybrid nanomaterials as a function of the PY/MoS_2 ratio.

3.1.4. Electrochemical analysis of MPY hybrid nanomaterial-based supercapacitor

Electrochemical performance of the MoS_2/PPY nanomaterials was investigated by cyclic voltammetry (CV). Beforehand, the MoS_2/PPY nanomaterials were dispersed in DI water at a concentration of 0.5 mg mL^{-1} by ultrasonic homogenizer with its amplitude of 30% for 30 min with an interval of 1 s for every sonication for 3 s. The dispersions were drop-casted onto the Au/PEN substrates and dried at 60 ℃ for at least 4 h in a convection oven. The CV curves were measured in the three-electrode system that the prepared electrodes were utilized as working electrodes, Ag/AgCl (in 3 M NaCl) as a reference electrode, Pt wire as a counter electrode, and H_2SO_4 aqueous solution (1 M) as an electrolyte.

To verify the electrochemical properties of the MoS_2/PPY nanomaterials, the CV curves were compared in **Figure 26a**. The CV was scanned at a same scan rate of 2 mV s^{-1} in the potential range of 0–0.9 V. Two distinctive peaks were the anodic peaks observed at 0.83–0.9 V, and the cathodic peaks at 0.15–0.2 V, and they are attributed to oxidation and reduction reactions of PPY, respectively [13]. The potential difference between the anodic and cathodic peak (or redox peak) was the least in the case of MPY_2.0, denoting the reduction of the overpotential required to overcome the electrical resistance of the nanomaterial.

The comparison of the specific capacitance among the MoS_2/PPY nanomaterials is displayed in **Figure 26b**. The specific capacitance was 94 and 120 F g^{-1} in the case of MPY_0.5 and MPY_1.0, respectively that almost no change occurred. The capacitance drastically increased to 312 F g^{-1} for MPY_2.0, in accordance with the aforementioned smallest redox peak difference and the increasing coverage of PPY layers on the MoS_2 nanosheets. The capacitance of MPY_5.0 and MPY_10 was lower than that of MPY_2.0, 202 and 255 F g^{-1}, respectively.

Figure 27 exhibits the galvanostatic charge-discharge (GCD) curves of MPY nanomaterials at a specific current of 0.5 A g^{-1} in terms of the PY/MoS_2 ratio. The result of the GCD curves are in a good agreement with that from CV curves. The specific capacitance of MPY_0.5 and MPY_1.0 was 21 and 76 F g^{-1}, respectively. Also, the capacitance was the highest, 252 F g^{-1} for MPY_2.0, and decreased with increasing PY/MoS_2 ratio. The MPY_5.0 and MPY_10 have their specific capacitance of 207 and 117 F g^{-1}, respectively, and the trend is almost same as that of CV curves, explaining the boost of the pseudocapacitive behaviors of PPY by hybridization with MoS_2.

Moreover, the rate capability of the MPY hybrid nanomaterials was examined by scanning CV with increasing scan rate from 2 to 250 mV s^{-1}. Rate capability can be identified by comparing the capacitance change in terms of scan rate. Therefore, the trend of the specific capacitance of MPY nanomaterials as a function of the scan rate is depicted in **Figure 28**. In specific, the capacitance value at 2 mV s^{-1} was divided by the capacitance at 250 mV s^{-1}. The MPY hybrid showed 12.3 to 25.2% of capacitance retention, while the pristine PPY had the retention of 7.5%. The dominance of the pseudocapacitance over EDLC for the PPY induces the diminution of the capacitance retention. On the contrary, the MPY hybrid nanomaterial represents enhanced retention, due to the improved electrochemical stability by PPY layers bonded with MoS_2 nanosheets.

Electrochemical impedance spectroscopy (EIS) was measured to scrutinize the electrochemical behaviors of the MPY nanomaterials deeply. **Figure 29** represents the Nyquist plot of the MPY nanomaterials being measured by applying 10 mV of alternating voltage, ΔV. When ΔI is an output of sinusoidal current, the electrochemical impedance $Z(w)$ is defined as follows,

$$Z(w) = \Delta V/\Delta I = Z'(w) + jZ''(w)$$

where w is the pulsation, $j = \sqrt{-1}$, while $Z'(w)$ and $Z''(w)$ are the real and imaginary parts of the impedance, respectively [76]. The greatest distinction between two EIS curves is the intercept of the abscissa. The x intercept indicates the internal resistance of the electrode material, and the intercept of the MPY was 3.59 Ω, while that of the pristine PPY was 3.92 Ω. In addition, a region between a vertical line (low frequencies) and x intercept (high frequencies) in the Nyquist plot with a 45° slope line is affected by physical parameters which influence the diffusion of electrolyte ions through the electrode materials. The 45°-sloped region of the graph of MPY is shorter than that of PPY, indicating that the capacitive behaviors of PPY are improved by hybridization with MoS_2 nanosheets.

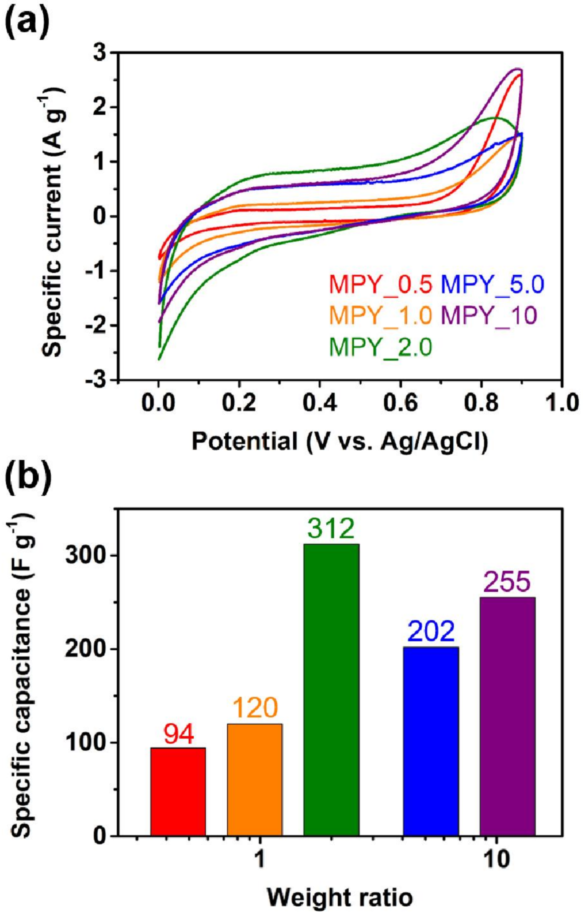

Figure 26. (a) CV curves of the series of MPY hybrid materials at a scan rate of 2 mV s^{-1} and (b) a comparison of specific capacitance of MPY

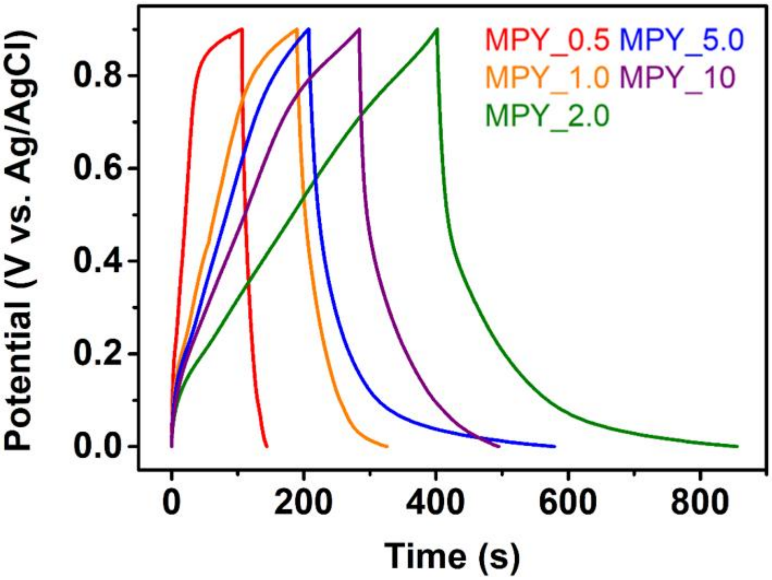

Figure 27. Comparison of GCD curves of the series of MPY hybrid nanomaterials at a specific current of 0.5 A g^{-1}.

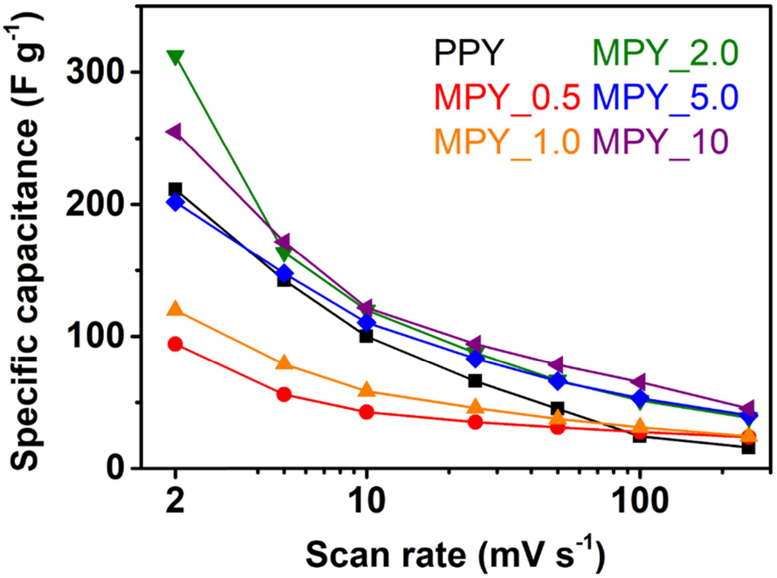

Figure 28. Rate capability of the series of MPY hybrid in the range of 2–250 mV s^{-1} of scan rate.

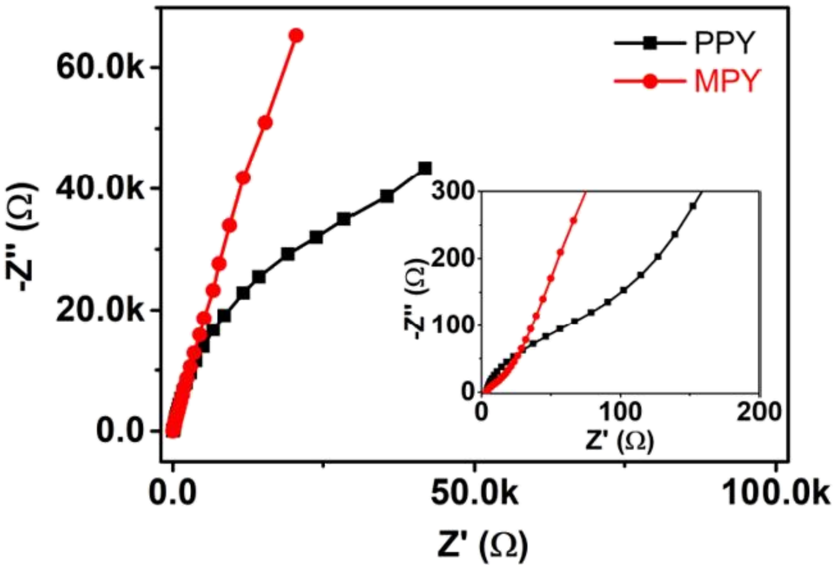

Figure 29. Nyquist plot of PPY (black) and MPY_2.0 (red); (Inset) High magnification of the Nyquist plot.

3.2. FPPY hybrid nanomaterials by covalent bonding

3.2.1. Fabrication of phosphorene from red phosphorus

Phosphorene was fabricated by phase transition of red phosphorus (RP) to black phosphorus (BP) and subsequent sonochemical exfoliation of BP. **Figure 30** depicts a schematic diagram of the fabrication of BP induced its phase transition from RP, an inexpensive precursor by mechanochemical ball mill process. Following ultrasonication induced the exfoliation, yielding the multilayer phosphorene. Ball mill process not only changed its shape of RP from a chunk to the flake but provoked the phase transition from amorphous (RP) to β-metallic (BP) phase [43].

The morphological change of the RP after the ball is presented by TEM in **Figure 31**. It is known that the size of 2D materials is controlled by mechanical milling, and it was confirmed by the change of morphology [77]. From the TEM images, the lateral size of RP was about 1.2 μm, and that of 24 h-milled BP was about 650 nm, indicating that the size of RP reduced significantly after the ball mill. Ultrasonic cavitation remarkably reduced its size along the plane direction for BP flakes. Still, with its shape remained the 2D structure after the exfoliation, the lateral size of the phosphorene was about 400 nm. From AFM images and their height profiles, the thickness of RP, BP, and phosphorene was also compared. The thickness of the RP precursor exceeds 100 nm, while it diminished after mechanical milling. In the case of the 24 h-milled BP, its thickness was above 60 nm. The thickness reduced to *ca.* 5 nm when it started to be exfoliated. Thus, it is proved that the few-layer phosphorene is successfully manufactured and the number of the layer is 6 [78].

The duration of mechanical milling was precisely controlled from 6 h to 36 h, and the powders turned their colors from mahogany red to black, implying that BP was successfully formed after the ball mill. In addition, the color of the prepared BP powder became darker with longer milling time until 18 h, and the change stopped at longer milling [79]. The color change of BP flakes depending on the duration of ball mill was pictured by digtal photographs in **Figure 32**.

XPS was selected to analyze the chemical states of the surface of the prepared BP flakes before and after the ball mill (**Figure 33**). P 2p core-level spectra of RP and the 24 h-milled BP after the ball mill were comapred. The characteristic peaks of RP after the deconvolution were positioned at 129.6 eV ($2p_{3/2}$) and 130.4 eV ($2p_{1/2}$) whose intensity ratio between two peaks was 2:1, in agreement with the theoretical value. The feature peaks of BP were revealed at 129.8 eV ($2p_{3/2}$) and 130.6 eV ($2p_{1/2}$), both shifted to higher binding energies. This peak shift can be a strong evidence that the mechanical milling of RP induces its phase transition to BP. A difference among the BPs depending on the duration of the ball mill was barely seen from the deconvolution results in **Figure 34**.

The structural information about the preparation of BP and phosphorene as a function of the duration of the ball mill and of the exfoliation, respsectively, was scrutinized by Raman spectroscopy (**Figure 35**). RP can be regarded as an intermediate phase between white and α-metallic violet phosphorus, and the structural subunits of violet phosphorus are proved to be present in amorphous RP. The major peak at 350 cm^{-1} is due to the stretching vibrations of P_8 and P_9 cages of amorphous RP [80]. The distortional modes of both P cages induced the small peak at 400 cm^{-1}, and the peak around 460 cm^{-1} produced by the combination of shear and breathing modes of the P cages was hardly detected.

The phase transition of RP to BP is motivated by the ball mill process. Mechanochemically induced phase transition, exhibiting three prominent characteristic peaks. They can be attributed to out-of-plane phonon mode (A_g^1) positioned at 359.6 cm^{-1} and two in-plane modes (B_{2g} and A_g^2) at 435.5 and 462.5 cm^{-1}, respectively. The intensity of the stretching vibrations of RP decreased while the A_g^1 peak appeared simultaneously, which is a clear proof of the phase transition. Still, the phase transition of RP was incomplete by the mechanical milling process itself. This can be explained by the presence of the shoulder in all A_g^1 peaks, being caused by the stretching vibrations of RP mentioned above [81,82].

The position of A_g^1 peak at 359.7 cm^{-1} is close to that of stretching vibration peak from RP at 350 cm^{-1}. Unlike A_g^1 peak, both B_{2g} and A_g^2 peaks are separated from the peak of stretching vibrations of violet phosphorus. When compared with the spectrum of RP, the intensity difference of the A_g^2 peak is more distinct than the B_{2g} peak. Consequently, all the spectra were normalized by the peak intensity of A_g^1 beforehand to compare the degree of the phase transition of ball-milled BPs in terms of milling time. In that case, 24 h-milled BP has the highest intensity of A_g^2 among all the BP flakes. In addition, the shoulder peak at 350 cm^{-1} near A_g^1 peak become smaller in the case of 24 h-milled BP. Accordingly, it can be deduced that milling of BP for 24 h is the optimum duration for the highest phase transition. The phase transition causes the crystal structure to change from the bulk to 2D structure, making BP easier to be exfoliated. Thus, the 24 h-milled BP was selected to the precursor of phosphorene previously.

Furthermore, the exfoliation effect to the chemical structure of BP flakes were examined in **Figure 36**. The phosphorene was fabricated by the LPE of the BP flakes using ultrasonication to produce large quantities, which is essential for commercialization [12]. To compare the exfoliation effect, Raman spectra were normalized against the intensity of A_g^1 peaks in the beginning. The shoulder of A_g^1 peak decreased for phosphorene comparing to the spectrum of BP. In addition, the exfoliation also induces an increment of the intensity of A_g^2 peaks. These implies that the ultrasonic cavitation during the exfoliation induces further phase transition ball-milled BPs. Moreover, in-plane vibrations inducing A_g^2 stiffens with decreasing the number of layers. Therefore, the comparison of the A_g^2 peak intensity can represent the thickness change of the BPs depending on the different duration of exfoliation. In other words, the decrease of the thickness during the exfoliation increases the intensity of A_g^2.

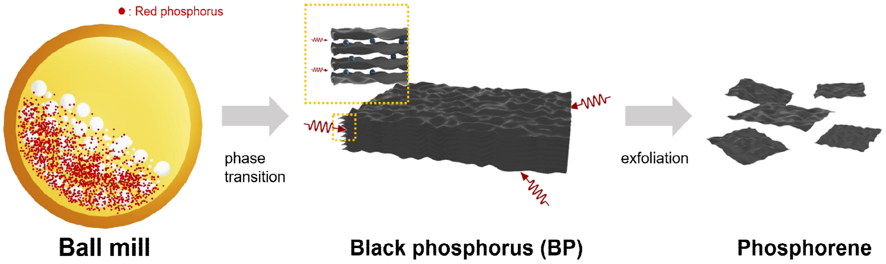

Figure 30. Schematic illustration of phase transition of BP from RP by ball mill and sonochemical exfoliation producing phosphorene.

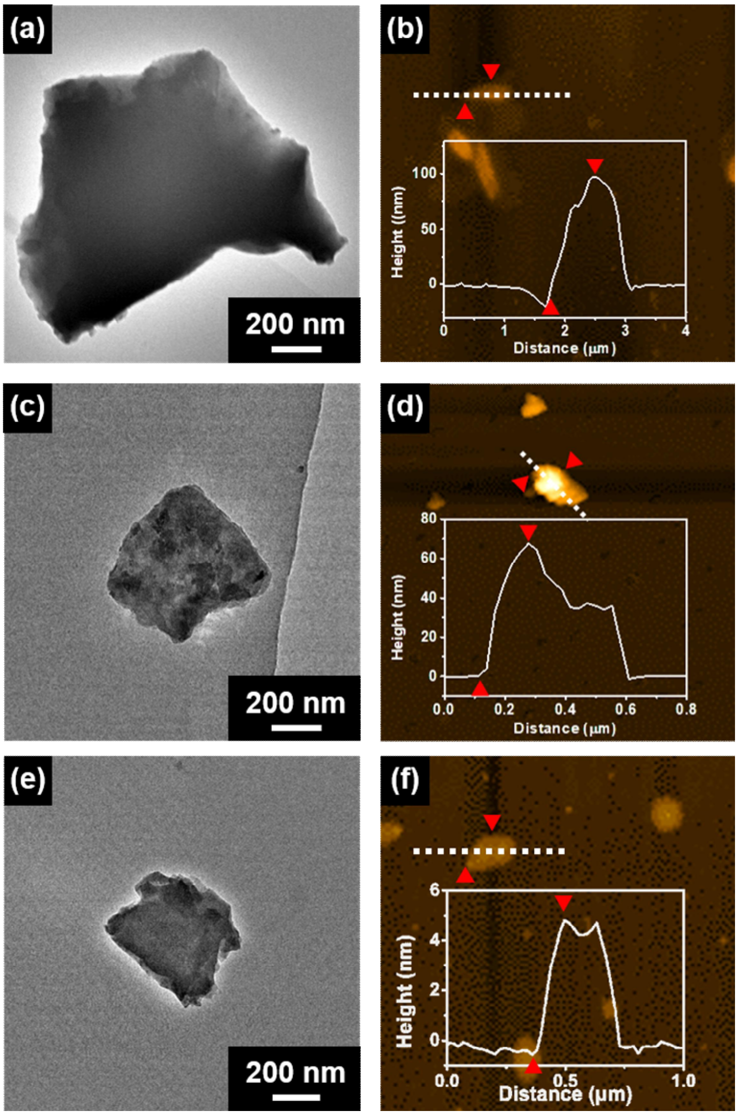

Figure 31. Morphological comparison of (a, b) RP, (c, d) BP, and (e, f) phosphorene by both TEM and AFM.

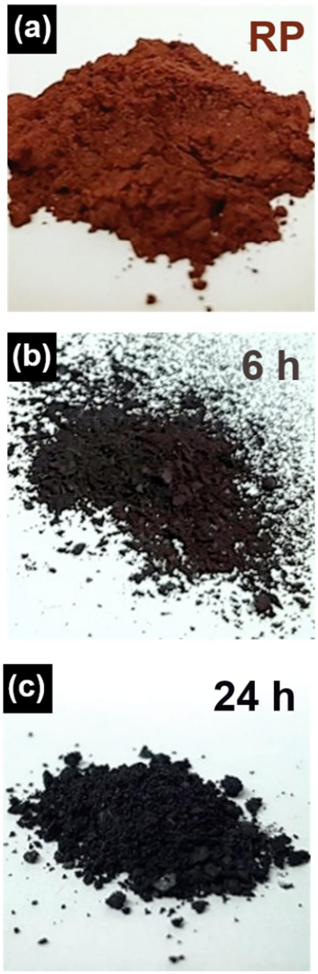

Figure 32. Digital pictures of RP (top), 6 h-milled BP (middle), and 24 h-milled BP (bottom).

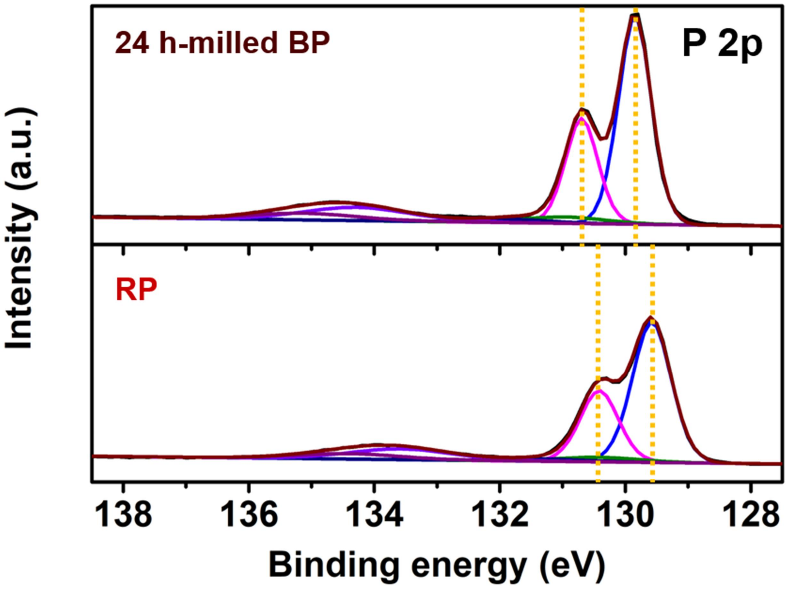

Figure 33. XPS spectra of P 2p orbital of RP (lower) and 24 h-milled BP (upper).

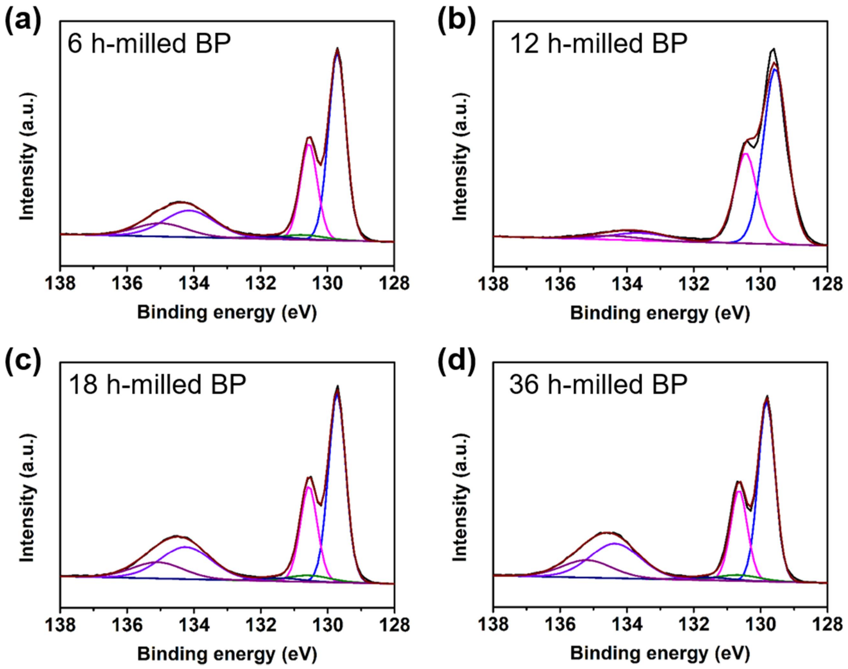

Figure 34. XPS spectra of P 2p orbital of (a) 6 h-, (b) 12 h-, (c) 18 h-, and (d) 36 h-milled BP.

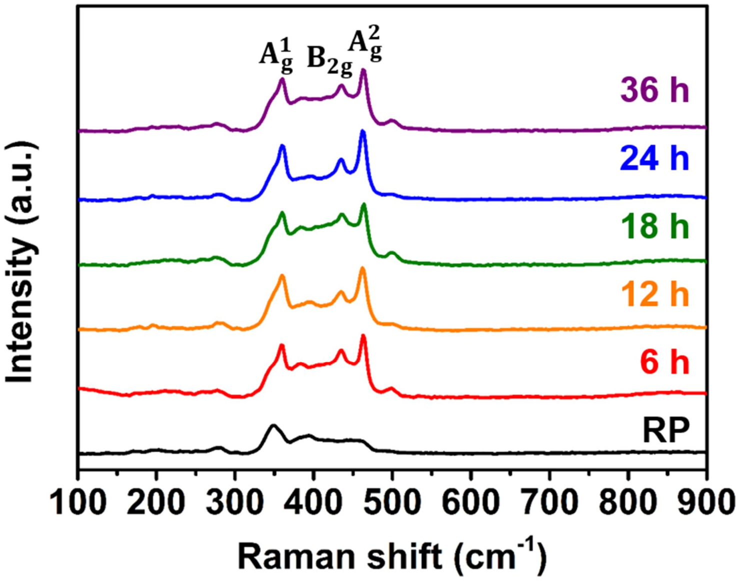

Figure 35. Raman spectra of RP and BP as a function of the duration of the ball mill.

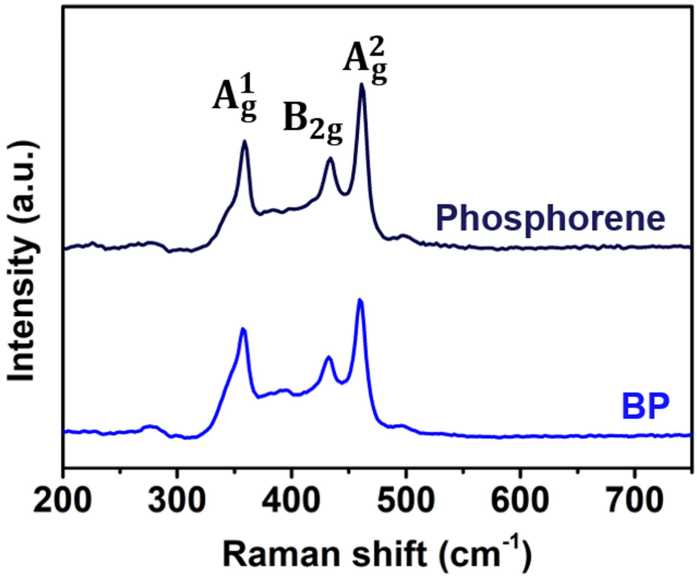

Figure 36. Raman spectra of 24 h-milled BP (lower) and phosphorene exfoliated for 2 h (upper).

3.2.2. Fabrication of FPPY hybrid nanomaterials and their characterization

The prepared phosphorene was mechanochemically functionalized by successive ball mill process. Enough energy for the functionalization with urea was supplied to the phosphorene by the mechanical milling. Urea was mixed with phosphorene with the weight ratio of 2:1. The functionalized phosphorene, denoted as FP, has a low stability against humidity, thus it was stored in a desiccator before usage. The prepared FP powder was first dispersed in DI water with a concentration of 1.0 mg mL^{-1} by sonication, and the mixture of pyrrole and pyrrole-3-carboxylic acid was put into the FP solution. The FP/PPY (FPPY) hybrid nanomaterials were fabricated by adding the initiator with a fixed value of molar ratio of $FeCl_3$ to monomer of 1.75 to maximize the electrical conductivity.

Figure 37 represents the TEM images of the FPPY hybrid nanomaterials, showing their morphological changes depending on the gravimetric ratio of pyrrole to FP. The functionalization of BP barely affects to the morphology of FP (**Figure 37a**), and the hybridization results in the conformal coating of spherical PPY. When the ratio of PY/FP is 1.0, it lacks reactants to formulate PPY layer with any structure (**Figure 37b**). The FPPY_2.0 shows somewhat hollow structures of PPY, and this may come from the polymerization location that the functionalization mainly occurs at the edges of the BPs. Full coverage of PPY nanospheres were detected for FPPY_5.0, and thicker PPY layers were coated for FPPY_10 and FPPY_20, due to higher ratio of PY/FP (**Figure 37c–f**).

The functionalization of phosphorene was analyzed by Fourier-transform infrared (FT-IR) spectroscopy. **Figure 38** displays the difference along the fabrication from the BP to FP, and to FPPY hybrid nanomaterials. Before the functionalization, the BP, prepared by the ball mill process of RP, displayed a sharp peak at 1632 cm^{-1}, which is due to the oxidation of phosphorus. Likewise, Minor peaks due to the oxidized phosphorus were also observed at 1384, 1050, and 577 cm^{-1}. The FT-IR spectrum of the FP revealed additional characteristic peaks ascribed to the P=O bonds at 1143, 493 cm^{-1} and P–O–C bonds at 1004 cm^{-1}, specifying that the phosphorene forms covalent bonds with urea [83]. The broad peak in the range of 1700–1500 cm^{-1} is attributed to deformation of N–H bonds from urea. The characteristic peaks of PPY were revealed dominantly in the case of the spectrum of the FPPY nanomaterials. The C=C, C=N in-plane vibrations, C–N peaks observed at 1526, 1452, and 1300 cm^{-1}, respectively, were by the PPY layer. The peaks at 1167 and 1044 cm^{-1} are assigned to C–H in-plane vibrations, and the peak at 787 cm^{-1} is attributed to the C–H out-of-plane bending vibrations from the pyrrole rings [84,85]. The most substantial peak of the spectrum of the FPPY nanomaterial is the amide bonds noticed at 1549 cm^{-1}. It is confirmed as a result of the reaction between the amine group of the FP and the carboxylic acid group of the monomer.

Raman spectroscopy was adopted to analyze the structural information of the FPPY hybrid nanomaterials deeply. All the samples were pelletized at a pressure of 7 metric ton to enhance its resolution. As represented in **Figure 39**, the Raman spectra of the FPPY hybrid nanomaterials as a function of the gravimetric ratio between pyrrole and FP mainly displays two peaks in the range of 1300–1600 cm^{-1} of Raman shift. When the ratio of PY/FP is 1 or larger, no peak from FP was observed in the Raman spectra, indicating that PPY fully wraps the FP substrate. In the case of FPPY_1.0, the small peaks at 928, 980 cm^{-1} were detected which are attributed to the ring deformations of the bipolaron and the polaron, respectively. The broad peak near 1051 cm^{-1} corresponds to the combination of the C–H in-plane deformation of PPY and the P–O–C symmetric stretching. As explained above, all the spectra showed two dominant peaks peaks in the range of 1300–1600 cm^{-1}. The appearance of the peaks at around 1340 and 1550 cm^{-1} arises from the ring stretching of the PPY backbone and the π-conjugated structures [70].

The ratio of the intensity of the peaks at 1340 and 1550 cm^{-1} (I_{1340}/I_{1550}) was compared in **Figure 40a**. The lowest value of the I_{1340}/I_{1550} was 0.90 for the FPPY_1.0, and it was increased to 0.98 and 1.02 for the FPPY_2.0 and FPPY_5.0, respectively. The I_{1340}/I_{1550} value of both the FPPY_10 and FPPY_20 was 1.0 that it does not change much from the FPPY_5.0. Along with the change of the intensity ratio, the shift of the peaks at 1340 and 1550 cm^{-1} is also compared. According to the **Figure 40b**, the trend of the peak shift is same as that of I_{1340}/I_{1550} ratio. It can be deduced that the I_{1340}/I_{1550} ratio as well as the peak shift are contingent on thickness of the PPY layers. Both peaks are shifted because of the N–C–N asymmetric stretching as well as amide I band, inducing the peak shift toward higher energies (blueshift) [86,87].

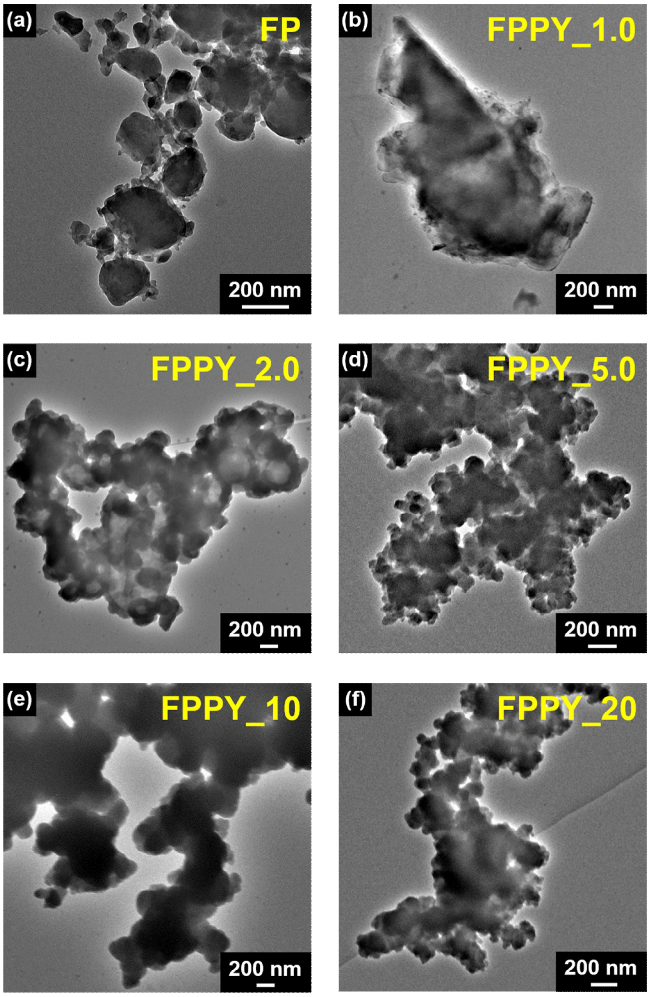

Figure 37. TEM images of (a) the FP and the series of FPPY hybrid nanomaterials whose PY/FP ratio is (b) 1.0, (c) 2.0, (d) 5.0, (e) 10, and (f) 20.

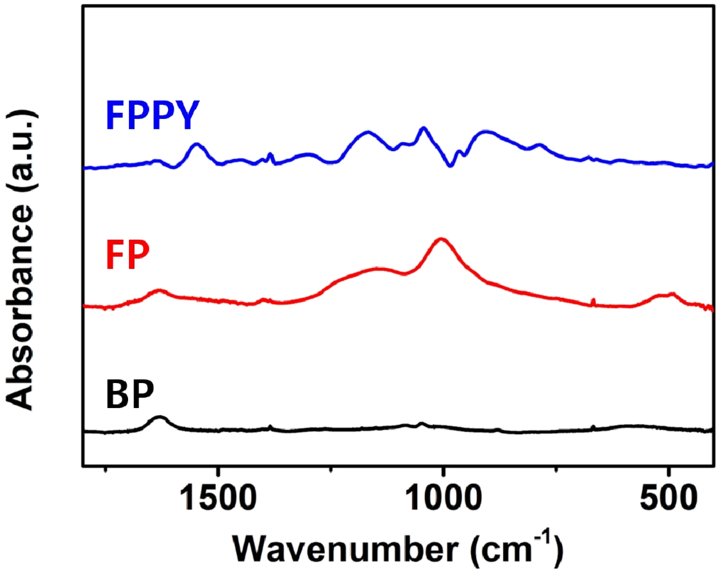

Figure 38. Comparison of the FT-IR spectra of BP (black), FP (red), and FPPY (blue).

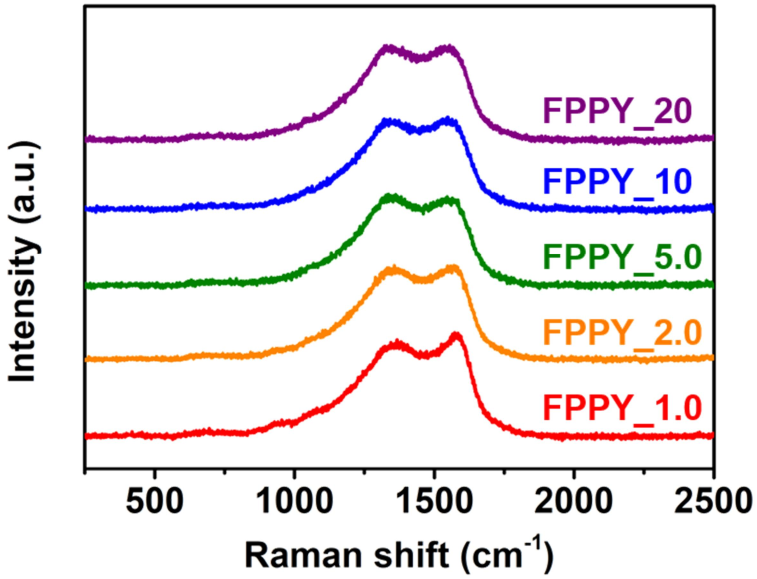

Figure 39. Raman spectra of a series of FPPY as a function of the PY/FP ratio.

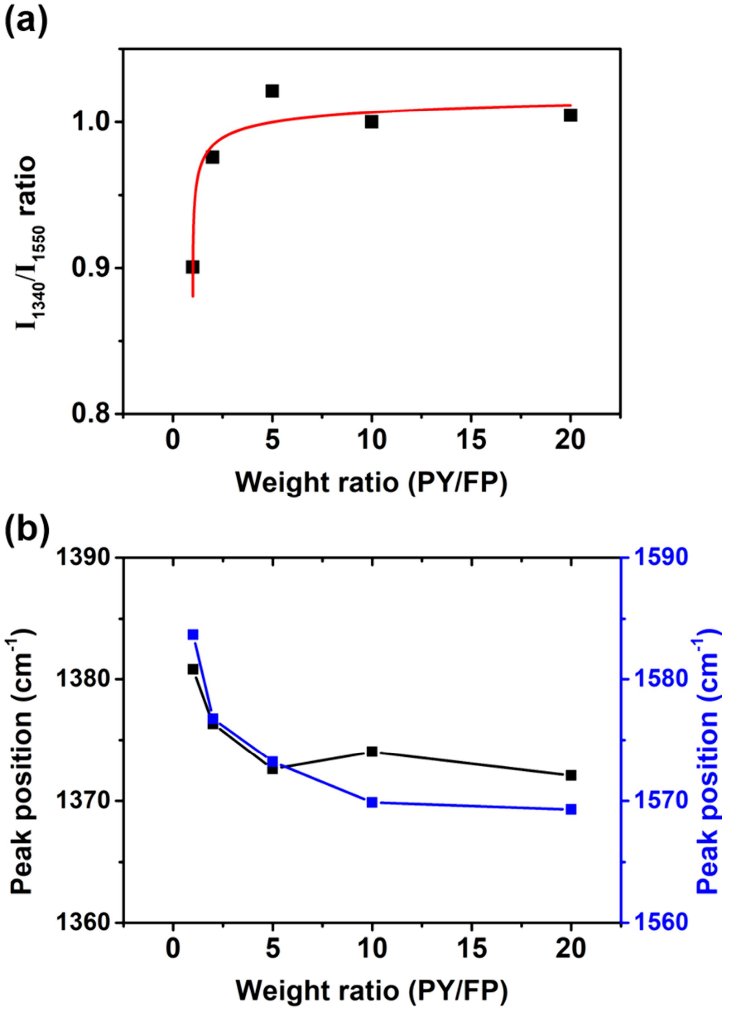

Figure 40. (a) The ratio of I_{1340}/I_{1550} and (b) the peak position as a function of the PY/FP ratio.

3.2.3. Electrochemical analysis of FPPY hybrid nanomaterial-based supercapacitor

Both the potentiostat and the galvanostat were utilized to verify the electrochemical behaviors of the FPPY hybrid nanomaterials. **Figure 41a** displays the CV curves of the FPPY hybrid nanomaterials with their weight ratio of PY to FP. The CV curves were obtained at a scan rate of 2 mV s^{-1} to distinguish all the electrochemical properties, as electrical double-layer capacitance becomes dominant at higher scan rates. Two peculiar peaks were the anodic peaks observed at 0.84–0.88 V, and the cathodic peaks at 0.15–0.2 V, which are attributed to oxidation and reduction reactions of PPY, respectively. As the PY/FP ratio increases, the area of CV curves increases until FPPY_5.0. The area diminishes for further increment of the PY/FP ratio. The change of the CV curve area is directly related to the supercapacitor performance, and **Figure 41b** shows a comparison of the specific capacitance of FPPY nanomaterials as a function of the PY/FP ratio. The specific capacitance of the FPPY_1.0 was 87.5 F g^{-1}, and an enhancement occurred for the FPPY_2.0, whose capacitance was 176.0 F g^{-1}. A drastic improvement of the capacitive behaviors was observed that the capacitance of the FPPY_5.0 was 411.5 F g^{-1}, close to four times of that of the pristine PPY whose capacitance was 106 F g^{-1}. The capacitance reduces with increasing PY/FP ratio that it was 160.0 and 106.2 F g^{-1} for the FPPY_10 and FPPY_20, respectively. The change of the potential difference between the anodic and the cathodic peak is the same as the change of the specific capacitance in terms of the PY/FP ratio. The altered coverage of PPY layer on the FP nanosheets as well as the the reduction of the overpotential may boost the performance owing to the hybridization.

EIS was used to characterize the electrochemical behaviors of the hybrid nanomaterials. **Figure 42** is the Nyquist plot in which the data from each frequency point is plotted by the imaginary part on the ordinate and the real part on the abscissa. The slope at low-frequency region of the FPPY is more vertical than that of the PPY, showing that the electrode material behaves closer to an ideal capacitor. At high frequencies, the R_{ct}, a charge-transfer resistance value slightly changed whose value of pristine PPY was 2.72 Ω, while that of FPPY hybrid was 2.61 Ω, as shown in the inset of the **Figure 42**. Moreover, the region in between the high and low frequencies, the length of 45° line of PPY was longer than that of FPPY, revealing that the capacitive behavior of FPPY is far improved by hybridization, comparing to the pristine PPY. Hence, all the factors of the FPPY hybrid overwhelm the pristine PPY, clarifying that the electrochemical behaviors of the FPPY hybrid nanomaterial is superior to the pristine PPY which may affect the performance of the electrode materials [88].

As mentioned previously, the excellent cycle stability is required for electrode materials in the practical implementation of energy-storage devices. The cycle stability was confirmed by CV with a scan rate of 25 mV s^{-1} to investigate the effect of the utilization, as described in **Figure 43**. The capacitance retention of the pristine PPY was only 27.5% after 500 cycles. On the contrast, the FPPY nanomaterial shows the improved capacitance retention of 56.5%, greater than double. The lower diffusion limitations as well as the enhancement of surface conductivity of the FPPY hybrid may strengthen the electrochemical stability comparing to the pristine PPY.

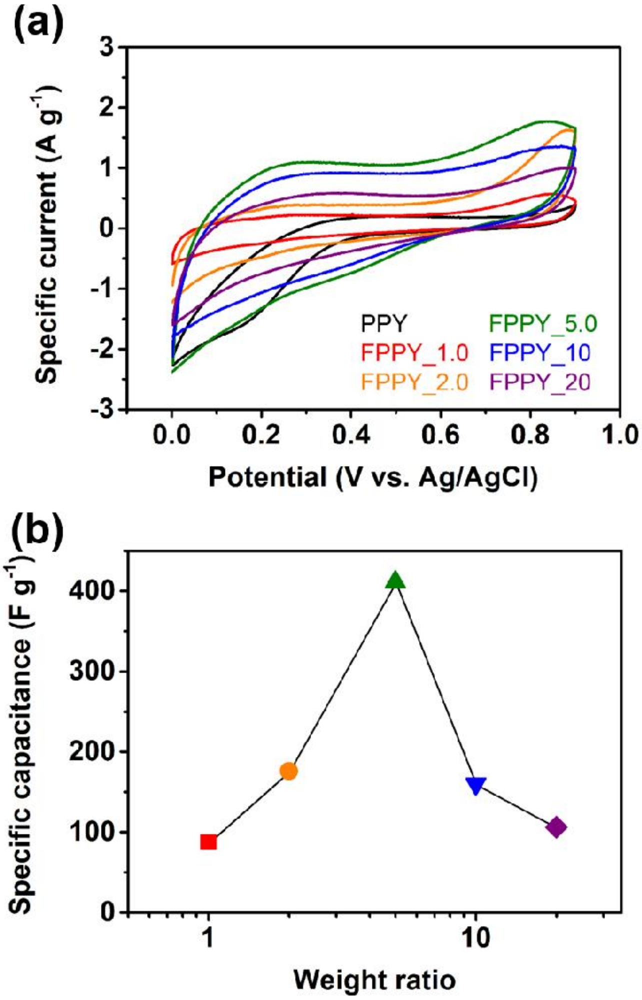

Figure 41. (a) CV curves of the series of FPPY hybrid materials at a scan rate of 2 mV s^{-1} and (b) a comparison of specific capacitance of FPPY as a function of the PY/FP ratio.

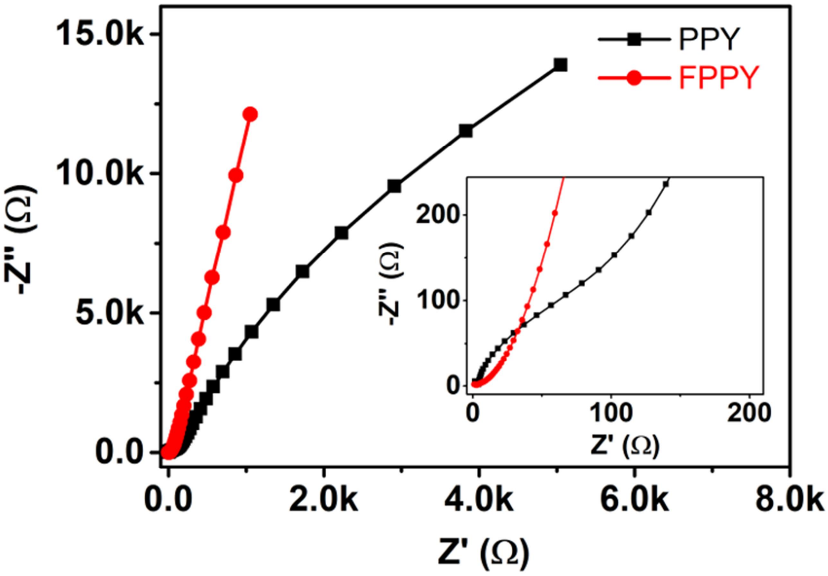

Figure 42. Nyquist plot of PPY (black) and FPPY_5.0 (red); (Inset) High magnification of the Nyquist plot.

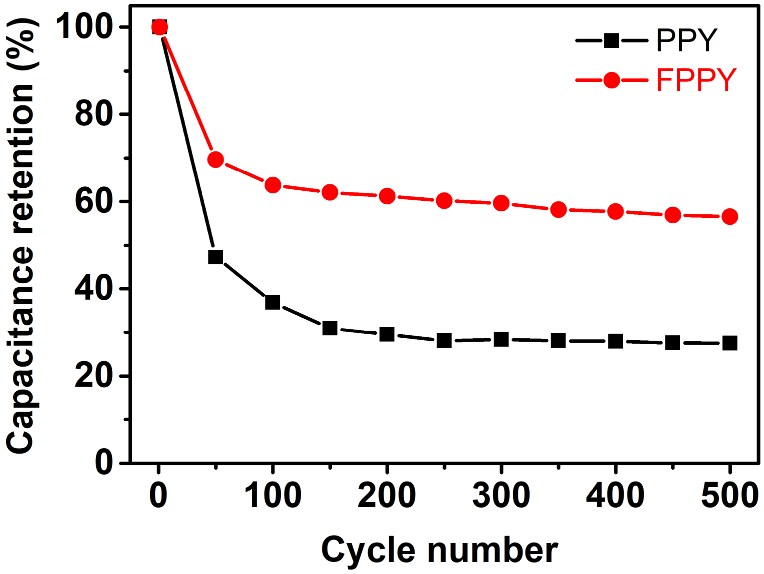

Figure 43. Cycle stability of PPY (black) and FPPY_5.0 (red) at a scan rate of 25 mV s^{-1}.

3.3. CVD-grown graphene/PPY hybrid nanomaterials by introduction of interfacial layer

3.3.1. Fabrication of CDPY hybrid nanomaterials

Vapor deposition polymerization (VDP) was adopted to fabricate CVD-grown graphene/PPY hybrid nanomaterials [89]. A schematic diagram of the fabrication of CDPY hyrid nanomaterials is depicted in **Figure 44**. An introduction of dopamine layer for controlling the polymerization of pyrrole produced a dopamine-assisted PPY grown on CVD-grown graphene, which denoted as CDPY. Depending on the type of initiator, either $FeCl_3$ or $CuCl_2$, the hybrid nanomaterial is denoted as CDPY-Fe or CDPY-Cu. According to the previous abbreviation, the nanomaterial without the introduction of dopamine is denoted as either CPY-Fe or CPY-Cu.

The FE-SEM images demonstrates the morphological control of PPY grown on dopamine-coated graphene. In the case of oth CPY-Fe and CPY-Cu, the prepared PPY after VDP partially covered the conductive substrate or aggregated irregularly with micron scale, as shown in **Figure 45**. Atmospheric O_2 plasma treatment seems to enhance its hydrophilicity of the surface, however, still the oxygen-containing groups after plasma treatment were not enough to spread all the initiators [90]. Meanwhile, the introduction of dopamine onto the graphene fairly enhanced the uniformity of initiator deposition. Comparison between the CPY and CDPY validates the effect of the deposition of dopamine that the PPY layers are deposited uniformly on its 2D substrate after VDP. On the surface of the CVD graphene are the PPY nanoparticles homogeneously deposited with the help of the inserted dopamine layers by the interactions between initiator cations and quinone moieties of dopamine [92–94]. From the FE-SEM images, it also indicates that the conducting polymer layers exhibit dramatic changes of their morphologies on the graphene depending on the type of the initiator. In fact, spherical PPY was deposited when ferric chloride was coated on the graphene, while the other initiator induced PPY to grow as nanoflakes, as in **Figure 45c**. In the case of CDPY-Fe, $FeCl_3$ led PPY to embellish the surface of the CVD graphene thoroughly as a form of spherical nanoparticles whose diameter is 80 ± 8 nm. In contrast, utilization of $CuCl_2$ made PPY grow anisotropically, as nanoflakes that the lateral size is about 500 nm (**Figure 45d**). This is to due the difference between the oxidation potential between two initiators [95]. As mentioned above, irrespective of the initiator species, nanoparticles or nanoflakes of PPY showed off their homogeneity on the surface of the graphene.

In addition, the effect of the concentration of dopamine solution was identified also in **Figure 46**. When the dopamine solution was not applied after coating the initiators, PPY became aggregated and grew into micron size, barely covered on the graphene in both cases. In the case of using $FeCl_3$ as an initiator, when the dopamine was spread on the graphene with relatively low concentration of 0.2 mg mL^{-1}, PPY nanospheres or nanoellipsoids with a wider size distribution (45–170 nm) were distributed sparsely on the graphene. When the higher concentration of dopamine (2.0 mg mL^{-1}) was applied, on the other hand, larger amount of dopamine molecules on the graphene made PPY accrete inconsistently and thickened the PPY layer. Meanwhile, the adoption of $CuCl_2$ led PPY to build into nanoflakes on the CVD-grown graphene. Irregular sizes of PPY flakes, in the range of 80–470 nm decorated the graphene when 0.2 mg mL^{-1} of dopamine was applied, while the CVD graphene was bedecked with bigger (about 800 nm) and denser PPY flakes when the concentration of dopamine was 2.0 mg mL^{-1}. As to dopamine concentration, the case of 1.0 mg mL^{-1} represented the highest uniformly, and according to this, this report will mainly cover the case of 1.0 mg mL^{-1} of dopamine to focus on the effect of applying dopamine to the polymerization of PPY with different initiators.

Surface roughness of the electrodes is to be available for energy storage, and crucial for a performance of super-capacitors. The electrode surface encounters the dielectric layer (electrolyte), playing a key role in supercapacitors. Hence, the average roughness of the surface depending on the initiators was identified by AFM. The AFM images of CDPY-Fe and CDPY-Cu in **Figure 47** with the same concentration of dopamine reveal considerable dissimilarity of their surface morphologies directly. When scanning the surface of CDPY-Fe, scores of PPY nanospheres with a dimeter of *ca.* 100 nm formed relatively smooth layer on the graphene, in a good agreement with FE-SEM image, and the value of RMS of CDPY-Fe was about 9.2 nm. In the case of the CDPY-Cu, however, it displayed diametric result comparing to CDPY-Fe. It has a bumpy layer consisting of PPY nanoflakes whose lengths are close to 500 nm. In addition, the RMS value of PPY layer was about 133 nm, more than 10 times larger than that of CDPY-Fe. It can be considered that this disparity of roughness may give a substantial influence to the performance of supercapacitor.

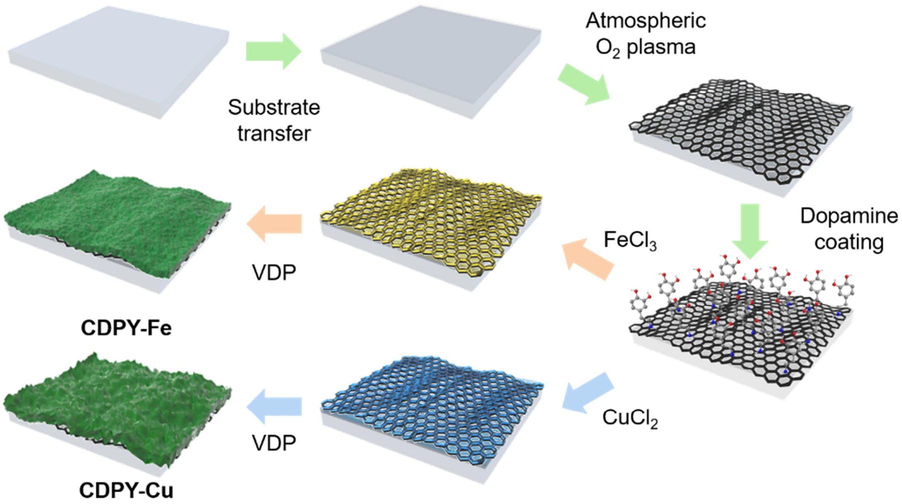

Figure 44. Fabrication scheme of CDPY hybrid nanomaterials by introducing dopamine layer and VDP process.

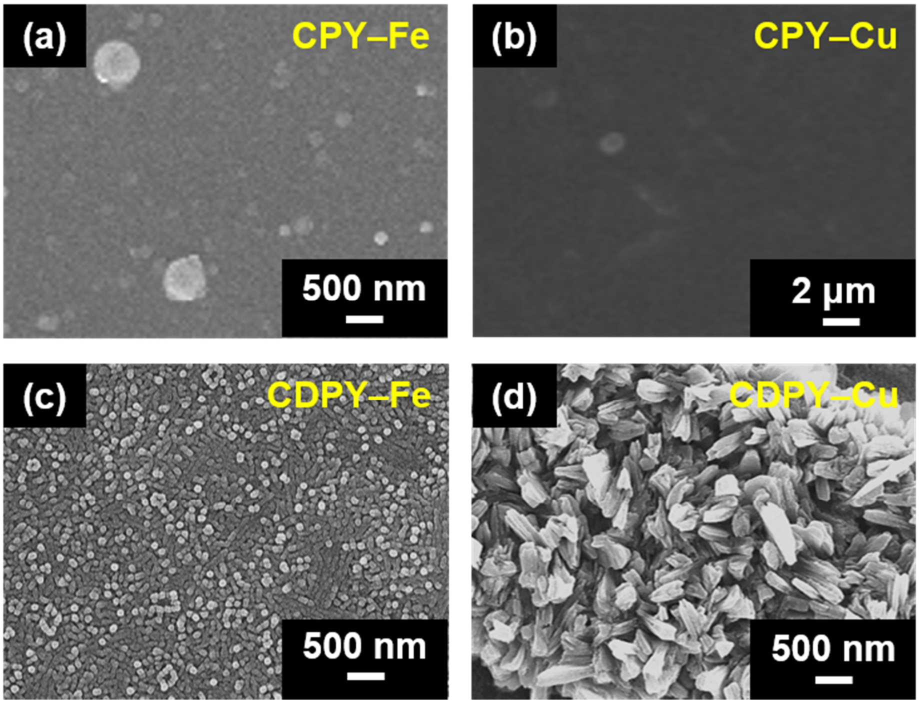

Figure 45. Comparison of the effect of introducing interfacial dopamine layer. FE-SEM images of (a) CPY-Fe, (b) CPY-Cu, (c) CDPY-Fe, and (d) CDPY-Cu.

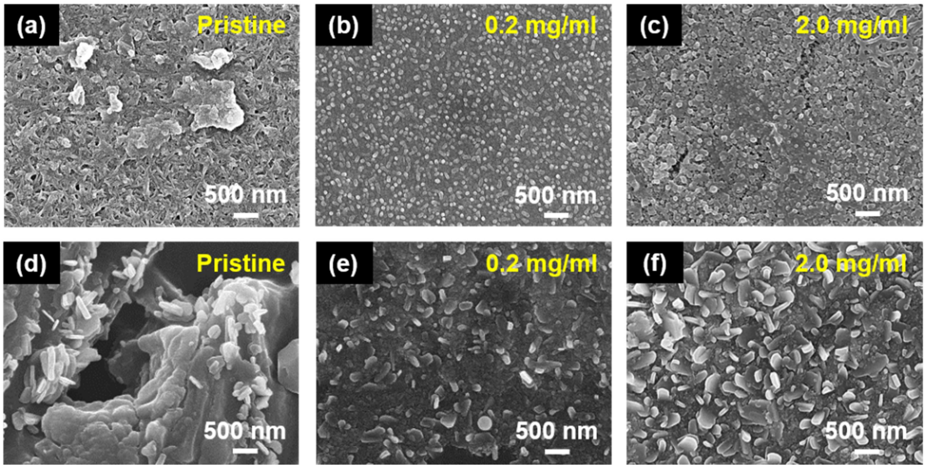

Figure 46. The effect of the concentration of dopamine to the morphology of PPY layers of CDPY hybrids. The concentration of dopamine solution is (a, d) 0, (b, e) 0.2 mg/mL, and (c, f) 2.0 mg/mL.

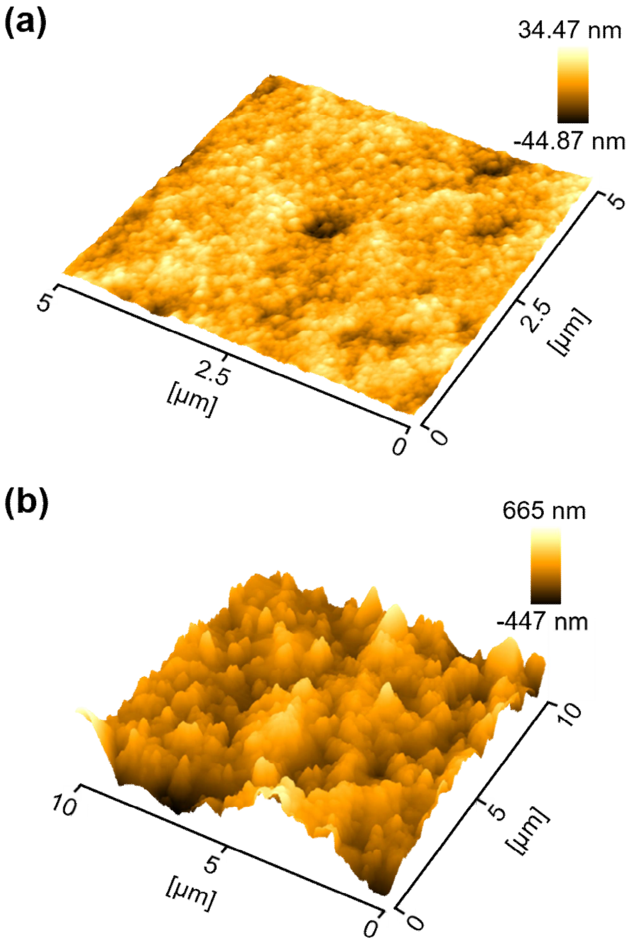

Figure 47. 3D AFM images of dopamine-treated (a) CDPY-Fe and (b) CDPY-Cu.

3.3.2. Material characterization of CDPY nanomaterials

Raman spectroscopy was adopted to identify chemical bonds of the CDPY nanomaterials by their inelastic scatterings of molecular vibrations using an excitation wavelength of 514 nm (**Figure 48**). Three prominent peaks of the CVD-grown graphene are D, G, and G′ bands. The so-called disorder-induced D band, originated by breathing modes of sp^2 carbon atoms in hexagonal rings at 1346 cm^{-1}, indicates the partial oxidation of graphene. The G band, observed at 1584 cm^{-1}, is due to the bond stretching of all pairs of sp^2 carbon atoms. As the second order of the D band, a single, sharp 2D band was appeared at 2683 cm^{-1} with higher intensity than that of G band [96–99].

In the case of the PPY, bipolaron and polaron structures of PPY induced two peaks at 935, 982 cm^{-1} by the ring deformation of bipolaron and polaron, respectively. The C–H in-plane bending vibrations of the reduction and oxidation states induced the peaks at 1057, 1080 cm^{-1}. The shoulder peak at 1248 cm^{-1} arises from N–H in-plane deformation. The C=C/C=N in-plane vibrations induce the peaks at 1369, 1412 cm^{-1}, and the reduction and oxidation states of C=C backbone the peaks at 1584, 1603 cm^{-1}, respectively [70].

XPS determines the chemical species consisting of CDPY materials (**Figure 49**). The C 1s core-level spectra of both materials, CDPY-Fe and CDPY-Cu, comprise five characteristic peaks whose binding energies are 284.5, 285.6, 286.4, 287.6, and 289.0 eV, attributed to C=C/C–C, C–N, C–OH, C=O, and C(=O)–N bonds, respectively [100,101]. The detection of the C(=O)–N peaks in both samples indicate that the dopamine molecules, by the reaction of amine groups with carboxyl groups of the graphene, connected well with the graphene. The intensities of both C=C/C–C and C–N peaks, originated from sp^2-hybridized carbons and PPY, are similar in CDPY-Fe and CDPY-Cu. However, the intensity of C–OH, C=O species were greater in CDPY-Cu than that in CDPY-Fe mainly due to the oxidation of PPY. It is evident that PPY polymerized by cupric chloride may be more vulnerable to the oxidation than that prepared by $FeCl_3$, since all fabrication steps were identical in both cases.

The N 1s spectra were further analysed to address the difference between CDPY-Fe and CDPY-Cu in depth. Deconvolution of two CDPY materials results in three components that correspond to three types of nitrogen atoms of the doped PPY. The peaks are at 398.5, 399.9, and 401.1 eV, and are attributed to imine (–N=) group, amine

(–NH–) group, and positively charged nitrogen polaron (–NH$^+$–), respectively [84,102]. The intensity of the polaron peak of PPY was greater in CDPY-Fe, whereas the intensity of imine groups was larger in CDPY-Cu.

It has been reported that the electronegativity of the initiators (dopants) affects the free carrier density and the activation energy for conduction of PPY. The additional states within the bandgap by the polarons generates the free carriers, and the activation energy for conduction decreases with the decrease in electronegativity of the initiators. From the deconvolution of N 1s spectra, percentage of the charged species of CDPY-Fe is about 36.5%, while that of CDPY-Cu is 16.5%. Based on the previous reports, the density of free carriers is clearly higher in CDPY-Fe than CDPY-Cu, due to the electronegativity difference between two initiators as mentioned previously [13,84]. In this manner, the CDPY-Fe possessed higher density of free carriers than CDPY-Cu. And along with the results of C 1s spectra, the degree of oxidations was also different, indicating PPY layers between two materials would display different features. Namely, it can be inferred that this difference may affect the performance as the electrodes of supercapacitor.

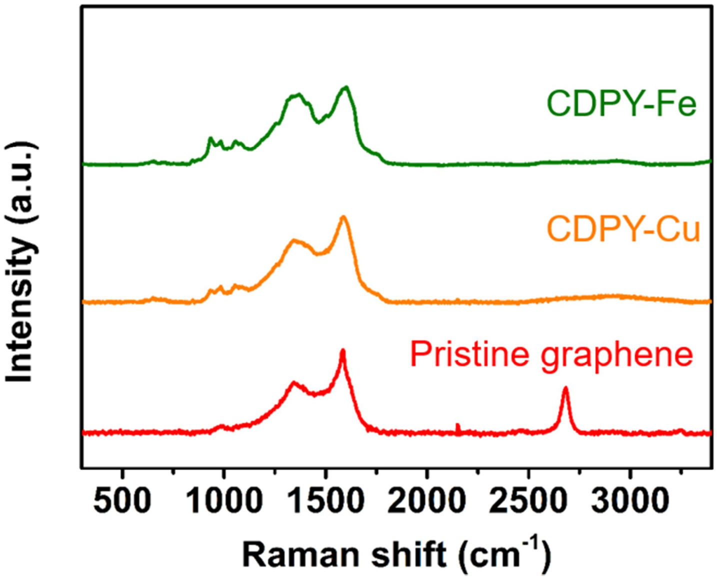

Figure 48. Raman spectra of (top, green) CDPY-Fe and (middle, orange) CDPY-Cu comparing to that of (bottom, red) CVD-grown graphene.

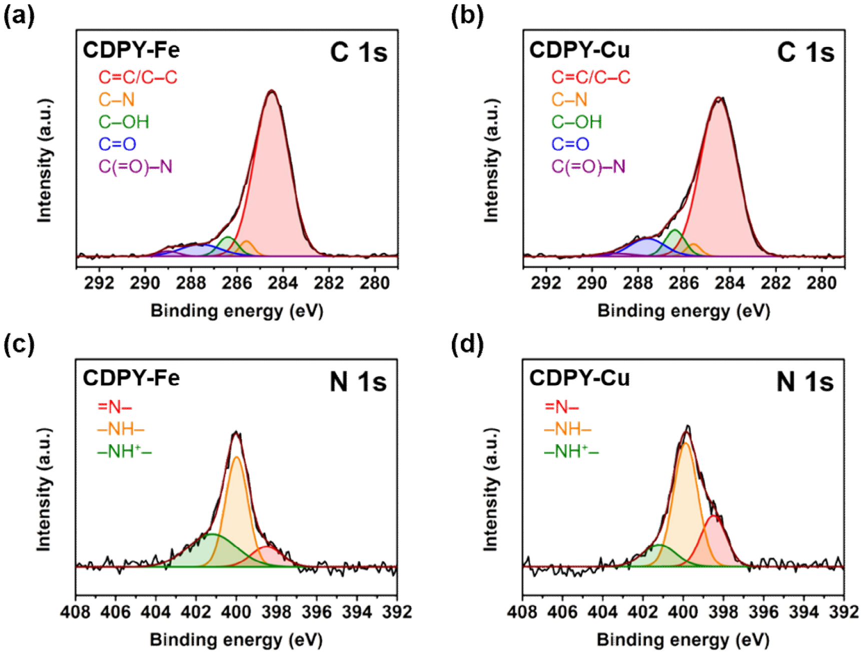

Figure 49. Deconvolution of XPS spectra of CDPy-Fe and CDPy-Cu composites. (a, b) C 1s spectra consist of five characteristic peaks, and (c, d) N 1s spectra consist of three characteristic peaks.

3.3.3. Electrochemical analysis of CDPY nanomaterials-based supercapacitor

Electrochemical properties of the CDPY-Fe and CDPY-Cu materials were investigated by cyclic voltammetry. The cyclic voltammograms (CVs) were measured in the three-electrode system whose electrolyte is H_2SO_4 aqueous solution, and in the case of CV traces, all the 3rd cycles were adopted equally for every case to analyse their electrochemical behaviours correctly. CDPY-Fe and CDPY-Cu on Au-sputtered polymer substrates were used as working electrodes, Ag/AgCl (in 3 M NaCl) as a reference electrode, and Pt wire as a counter electrode.

First, the CVs of both the CDPY-Fe and CDPY-Cu were compared at a low scan rate of 2 mV s^{-1} (**Figure 50**). In the case of CDPY-Fe, a distinct reduction and oxidation peaks appeared at ~ 0.4 V vs. Ag/AgCl, whereas no peak was observed in CDPY-Cu [102]. The detection of redox couples indicates its electrochemical activity of PPY layer, revealing that CDPY-Fe presented redox-active characteristics of PPY, while CDPY-Cu did not. From the XPS data, it was confirmed that the free carrier density of CDPY-Fe was greater than that of CDPY-Cu, and CDPY-Cu was larger than CDPY-Fe in the degree of oxidation. In accordance with XPS data, the discrepancy of redox peaks by PPY layers in these two materials emanates from the fact that the PPY layer of CDPY-Fe preserves the redox-active species, au contraire that of CDPY-Cu became less active through the oxidations. As a result, at a scan rate of 2 mV s^{-1}, the areal capacitance of CDPY-Fe is 3.15 mF cm^{-2}, albeit that of CDPY-Cu is 2.19 mF cm^{-2}, representing a superior performance comparing to pristine CVD graphene. The dopamine-omitted CPY materials have smaller areal capacitance, which is 1.16 and 1.51 mF cm^{-2} for CPY-Fe and CPY-Cu, respectively. GCD curves of the materials were characterized to compare their electrochemical behaviours in terms of the dopamine pretreatment and the species of oxidants at a same current density of 0.1 mA cm^{-2} (**Figure 51**). The areal capacitance of the CDPY-Fe and the CDPY-Cu is 3.15 and 2.20 mF cm^{-2}, whose trend is identical as that from CV curves.

However, such a predominance flipped at higher scan rates (**Figure 52**). The CVs of CDPY-Fe and CDPY-Cu with a change of the scan rate from 2 to 100 mV s^{-1} changed their shapes as the scan rate increased. The CV curves become close to the rectangular shapes in that case since the higher scan rates in voltammetry, the more dominant the EDLC is. As a measuring with increasing scan rate, asymmetric curves came out in the case of CDPY-Fe, while the CVs maintained their rectangular shapes in the case of CDPY-Cu even at 100 mV s^{-1}. Moreover, the capacitance of CDPY-Fe became smaller than that of CDPY-Cu at the same time. The capacitance of CDPY-Fe and CDPY-Cu was 0.47 mF cm^{-2} and 0.87 mF cm^{-2} at 100 mV s^{-1}, respectively. Capacitance retention of CDPY-Cu was far greater than that of CDPY-Fe. The scan rate may change the absolute values of capacitance, but the trend is mostly consistent. Thus, this trend change is of particular result. A single component cannot cause this change depending on the scan rates. The oxidation degree of PPY layer and the RMS difference as well as the charge carrier density between two CDPY materials are strong candidates of this result.

The CDPY-Fe has a greater density of free carrier than CDPY-Cu, thus the capacitance of CDPY-Fe exceeds at lower scan rates. Highly oxidized and crumpled PPY layer of CDPY-Cu performed a key role at higher scan rates. Charge storage mechanism of supercapacitor can be divided into two mechanisms, a faradaic reaction mechanism from diffusion-controlled charge transfer process and nonfaradaic mechanism from double-layer capacitance. When evaluated total stored charges, the latter is proportional to the scan rate, and the former is proportional to the square root of the scan rate. And this relationship between two mechanisms results in the shape of CVs as above mentioned. Consequently, the discrepancy of redox peaks by PPY layer in these two materials emanated from whether PPY layer is electrochemically active or not. Moreover, although CDPY-Fe has a larger number of free carriers than CDPY-Cu, CDPY-Cu with wider interfacial area between the electrode and the electrolyte exceeds the supercapacitor performance at higher scan rates.

Moreover, EIS was adopted to scrutinize the reason of their performance of CDPY materials depending on the scan rate in detail. The frequency response was measured by applying a low amplitude of alternating voltage (ΔV) of 10 mV. As ΔI being a sinusoidal output current, the electrochemical impedance $Z(w)$ is defined as follows,

$$Z(w) = \Delta V/\Delta I = Z'(w) + jZ''(w)$$

where w is the pulsation, $j = \sqrt{-1}$, while $Z'(w)$ and $Z''(w)$ are the real and imaginary parts of impedance, respectively. And the loss tangent, the ratio of dielectric loss and the real permittivity, is given as follows,

$$\tan\delta = Z'/Z''$$

Figure 53a is the Nyquist plot of supercapacitor cell assembled with H_2SO_4 aqueous solution electrolyte. Comparing with the CPY nanmaterials, the R_{ct} (charge-transfer resistance) values lowered when it comes to the CDPY nanomaterials. This clearly indicates that the adoption of dopamine layer enhances the charge transfer reaction between the PPY layer and the CVD-grown graphene. At low-frequency region of the Nyquist plot, the imaginary part of the AC impedance dramatically increases. The line more vertical at low frequencies indicates that the device is closer to an ideal capacitor. According to the low-frequency regions of the Nyquist plot, comparing to CPY-Fe, the slope of the low-frequency line lowered in the case of CDPY-Fe, while the slope showed an increment when CDPY-Cu was compared with CPY-Cu. This difference implies that the adoption of dopamine boosts the diffusion process when the PPY was deposited by $CuCl_2$, while the capacitive behavior is obstructed when using $FeCl_3$. This variance is in accordance with CV curves in **Figure 52** showing a “flipped” performance at high scan rate depending on the type of the initiator. This can be further explained by loss tangent plot in **Figure 53b**. A relaxation time, a minimum time required to discharge all the energy with an efficiency of greater than

50%, was shifted backward in the same order of decreasing the slope at low frequencies from the EIS curves in the Nyquist plot. The increase of relaxation time proves the increment of diffusion time constant, thus the diffusional system of CDPY-Fe nanomaterial has the largest hindrance [103,104].

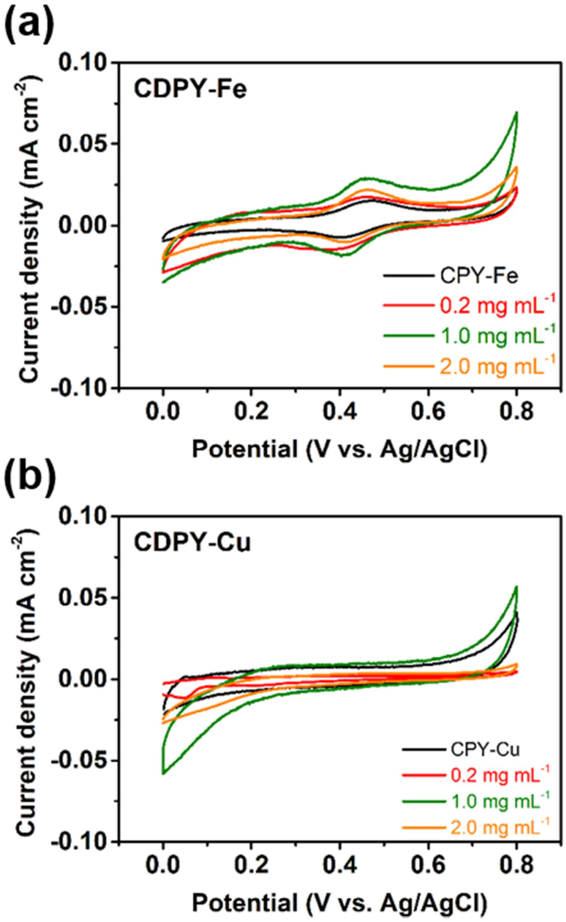

Figure 50. CV curves of (a) CDPY-Fe and (b) CDPY-Cu hybrids as a function of the precursor concentration of interfacial layer.

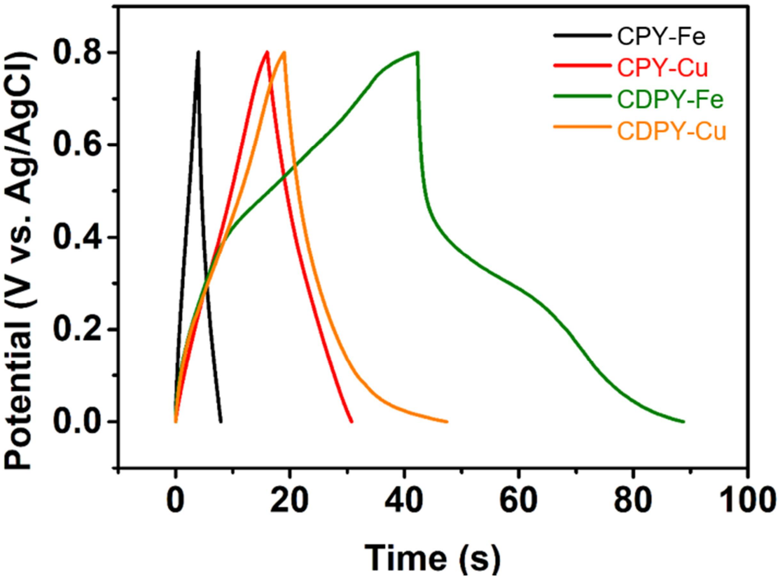

Figure 51. GCD curves of CPY-Fe, CPY-Cu, CDPY-Fe, and CDPY-Cu at a specific current of 0.5 A g^{-1}.

.

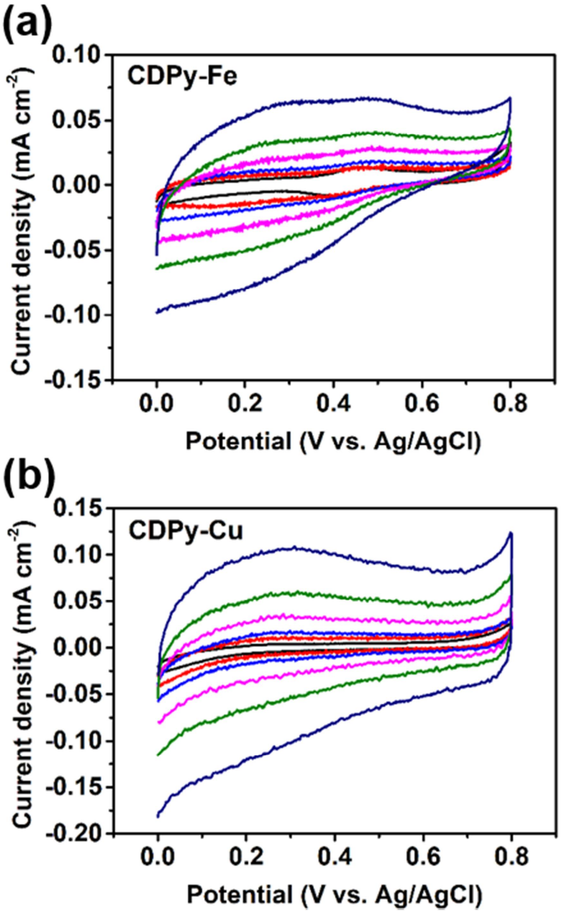

Figure 52. CV curves of (a) CDPY-Fe and (b) CDPY-Cu depending on the concentration of the precursor solution of interfacial layer.

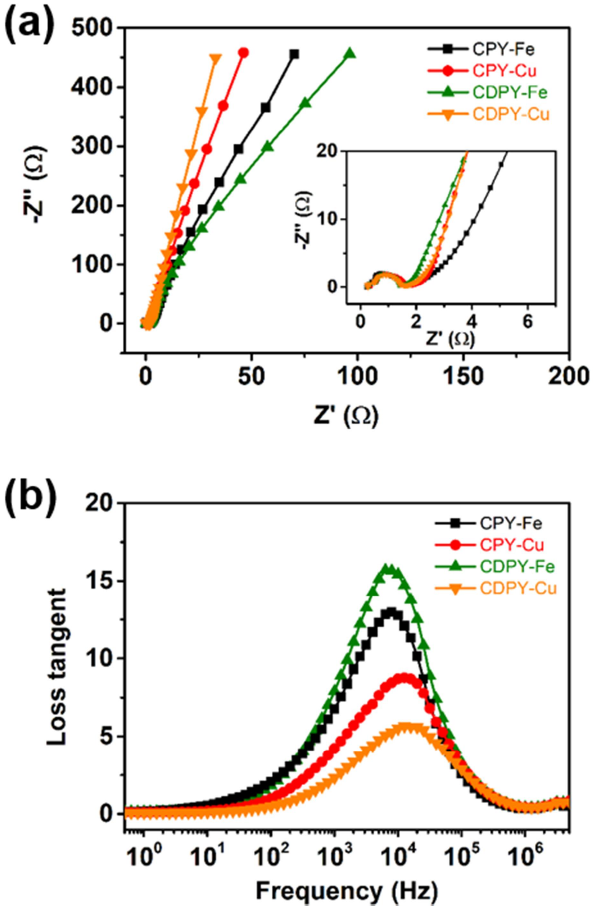

Figure 53. (a) Nyquist plot and (b) loss tangent plot of CPY-Fe, CPY-Cu, CDPY-Fe, and CDPY-Cu.

3.3.4. Performance of CDPY nanomaterials-based all-solid-state flexible supercapacitor

Figure 54a shows a digital picture of all-solid-state full-cell device of CDPY-Fe hybrid nanomaterial. The PVA/H_2SO_4 film was utilized as the solid electrolyte, and the film was sandwiched by two CDPY-Fe electrodes. The device was slightly pressed, and was sealed by PTFE film to keep moisture from evaporating. The full-cell device was stable with its bending radius of 0.5 cm. The full-cell device was measured at a voltage range of 0 to 0.8 V at a scan rate of 100 mV s^{-1}. As shown in **Figure 54b**, both the flat state and the bend state has almost same shape of CV curves, describing the high flexibility of the CDPY nanomaterial-based full-cell device.

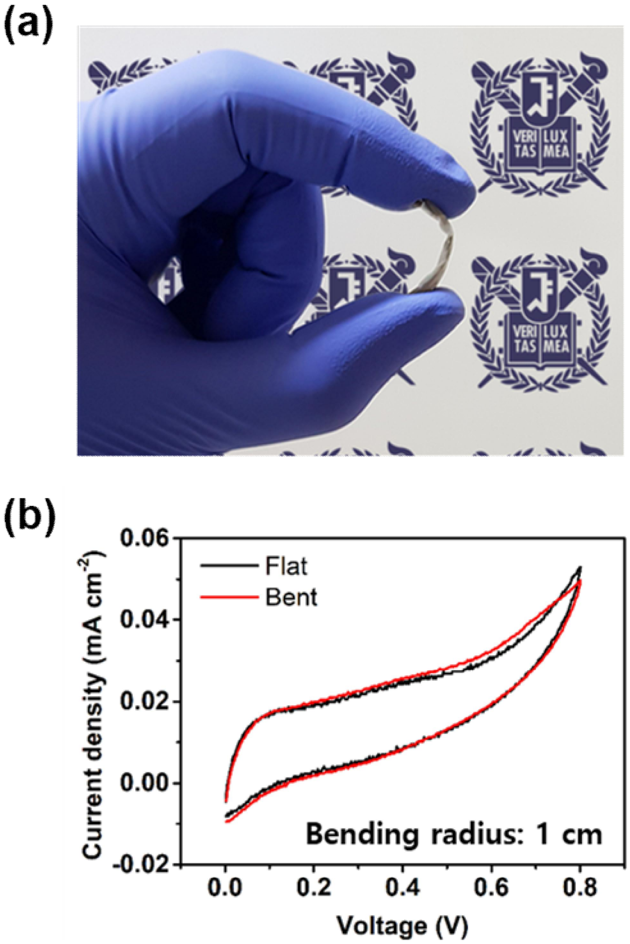

Figure 54. (a) A photograph of bent all-solid-state full-cell device of CDPY-Fe hybrid. (b) The comparison of CV curves of the full-cell device with flat (black) and bent (red) states.

4. Conclusion

PPY-based two-dimensional (2D) hybrid nanomaterials (MPY, FPPY, and CDPY) were manufactured successfully by integrative chemistry and applied to supercapacitor electrode materials. Adjusting the population and morphology of PPY layers grown on the various sturdy 2D nanomaterials (MoS_2 nanosheet, phosphorene, and CVD-grown graphene) was achieved by fabrications through non-covalent bonding, covalent bonding, and introducing interfacial layer, respectively. All the PPY-based hybrid nanomaterials exhibited improved supercapacitor performance as well as electrochemical behaviors. The subtopics are concluded in terms of each subtopic as follows:

1. MPY hybrid nanomaterials were fabricated by exfoliation of MoS_2 nanosheets from bulk MoS_2 and subsequent hybridization of PPY. By utilizing few-layer MoS_2 nanosheets as builing units of the hybrid material, non-covalent bonding between MoS_2 and pyrrole monomers induced MPY hybrids with a uniform decoration of PPY layer. During the oxidative polymerization, Mo–N bonding was created in between the MoS_2 and PPY, and the surface conductivity was ameliorated consequently. In addition, both the electrochemical

behaviors as well as rate capability of MPY were improved by lowering the diffusion hurdles compared to those of the pristine PPY.

2. Mechanical milling process induced phase transition of RP to BP as well as functionalization of the phosphorene which was prepared through sonochemical exfoliation of the prepared BP. The amine groups of phosphorene functionalized by urea and the carboxylic acid groups of pyrrole monomer mixtures formed amide bonds, thus FPPY hybrid was fabricated with the control of population and morphology of PPY layer. The intensity ratio between two dominant peaks at Raman spectra and also their peakshifts drew a conclusion that PPY layer was completely covered the FP substrates when PY/FP was 5.0. Moreover, the specific capacitance of the FPPY hybrid nanomaterials exceeded 400 F g^{-1}, because of the lowered penetration resistance of the electrolyte along with the diffusion kinetics.

3. The introduction of dopamine as an interfacial layer in between CVD-grown graphene and PPY improved the electrochemical behaviors of CDPY hybrid nanomaterials. Two types of initiators

($FeCl_3$ and $CuCl_2$) were utilized during the VDP process, and the difference of oxidation potential between them produced spherical and flakey PPY layers, respectively. As a result, the average roughness, the concentration of polaron of PPY was differed, inducing peculiar electrochemical behaviors respectively. The CDPY-Fe had lower value of the R_{ct} than the CDPY-Cu, thus the areal capacitance of CDPY-Fe was far greater than CDPY-Cu at a slow scan rate. On the contrary, they showed different capacitive behaviors at higher scan rate that the better diffusions of the electrolyte as well as smaller relaxation time of CDPY-Cu induced better performance than CDPY-Fe.

References

[1] A. J. Heeger, *Rev. Mod. Phys.* **2001**, *73*, 681-700.

[2] A. G. MacDiarmid, *Rev. Mod. Phys.* **2001**, *73*, 701-712.

[3] M. Rohwerder, *Int. J. Mat. Res.* **2009**, *100*, 1331.

[4] K. S. Ryu, Y.-G. Lee, Y.-S. Hong, Y. J. Park, X. Wu, K. M. Kim, M. G. Kang, N.-G. Park, S. H. Chang, *Electrochim. Acta* **2004**, *50*, 843-847.

[5] G. A. Snook, P. Kao, A. S. Best, *J. Power Sources* **2011**, *196*, 1-12.

[6] S. I. Cho, S. B. Lee, *Acc. Chem. Res.* **2008**, *41*, 699-707.

[7] F. Zhao, Y. Shi, L. Pan, G. Yu, *Acc. Chem. Res.* **2017**, *50*, 1734-1743.

[8] T. K. Das, S. Prusty, *Polym.-Plast. Technol. Eng.* **2012**, *51*, 1487-1500.

[9] J. M. P.J. Kinlen, Y. Kim, J. Jung and S. Viswanathan, *ECS Trans.* **2010**, *25*, 157-162.

[10] L. Nyholm, G. Nystrom, A. Mihranyan, M. Stromme, *Adv. Mater.* **2011**, *23*, 3751-3769.

[11] M. A. B. Kumaran Ramanathan, Minhee Yun, Wilfred Chen, Nosang V. Myung, and Ashok Mulchandani, *J. Am. Chem. Soc.* **2005**, *127*, 496-497.

[12] M. M. E. Benseddik, J.C. Bernede, S. Lefrant, A. Pron, *Synth. Met.* **1995**, *72*, 237-242.

[13] H. Han, J. S. Lee, S. Cho, *Polymers* **2019**, *11*, 232.

[14] K. Lota, V. Khomenko, E. Frackowiak, *J. Phys. Chem. Solids* **2004**, *65*, 295-301.

[15] H. S. Abdullah, *Int. J. Phys. Sci.* **2012**, *7*, 5468-5476.

[16] O. N. E. T V Vernitskaya, *Russ. Chem. Rev.* **1997**, *66*, 443-457.

[17] S. H. Cho, K. T. Song, J. Y. Lee, *in Handbook of Conducting Polymers, 3rd ed.: Conjugated polymers theory, synthesis, properties, and characterization (Eds.: T. A. Skotheim, J. R. Reynolds),* CRC Press Taylor & Francis Group*,* **2007**.

[18] P. Camurlu, *RSC Adv.* **2014**, *4*, 55832-55845.

[19] H. Zhang, *ACS Nano* **2015**, *9*, 9451-9469.

[20] J. Kang, V. K. Sangwan, J. D. Wood, M. C. Hersam, *Acc. Chem. Res.* **2017**, *50*, 943-951.

[21] A. C. Ferrari, F. Bonaccorso, V. Fal'ko, K. S. Novoselov, S. Roche, P. Boggild, S. Borini, F. H. Koppens, V. Palermo, N. Pugno, J. A. Garrido, R. Sordan, A. Bianco, L. Ballerini, M. Prato, E. Lidorikis, J. Kivioja, C. Marinelli, T. Ryhanen, A. Morpurgo, J. N. Coleman, V. Nicolosi, L. Colombo, A. Fert, M. Garcia-Hernandez, A. Bachtold, G. F. Schneider, F. Guinea, C. Dekker, M. Barbone, Z. Sun, C. Galiotis, A. N. Grigorenko, G. Konstantatos, A. Kis, M. Katsnelson, L. Vandersypen, A. Loiseau, V. Morandi, D. Neumaier, E. Treossi, V. Pellegrini, M. Polini, A. Tredicucci, G. M. Williams, B. H. Hong, J. H. Ahn, J. M. Kim, H. Zirath, B. J. van Wees, H. van der Zant, L. Occhipinti, A. Di Matteo, I. A. Kinloch, T. Seyller, E. Quesnel, X. Feng, K. Teo, N. Rupesinghe, P. Hakonen, S. R. Neil, Q. Tannock, T. Lofwander, J. Kinaret, *Nanoscale* **2015**, *7*, 4598-4810.

[22] Y. Chen, K. Yang, B. Jiang, J. Li, M. Zeng, L. Fu, *J. Mater. Chem. A* **2017**, *5*, 8187-8208.

[23] P. K. Kannan, D. J. Late, H. Morgan, C. S. Rout, *Nanoscale* **2015**, *7*, 13293-13312.

[24] F. Bonaccorso, A. Bartolotta, J. N. Coleman, C. Backes, *Adv. Mater.* **2016**, *28*, 6136-6166.

[25] X. Peng, L. Peng, C. Wu, Y. Xie, *Chem. Soc. Rev.* **2014**, *43*, 3303-3323.

[26] F. Yin, B. Gu, Y. Lin, N. Panwar, S. C. Tjin, J. Qu, S. P. Lau, K.-T. Yong, *Coord. Chem. Rev.* **2017**, *347*, 77-97.

[27] K. F. Mak, C. Lee, J. Hone, J. Shan, T. F. Heinz, *Phys. Rev. Lett.* **2010**, *105*, 136805.

[28] R. G. a. Q. Zhang, *ACS Nano* **2014**, *8*, 4074-4099.

[29] G. Eda, H. Yamaguchi, D. Voiry, T. Fujita, M. Chen, M. Chhowalla, *Nano Lett.* **2011**, *11*, 5111-5116.

[30] J. Zheng, H. Zhang, S. Dong, Y. Liu, C. T. Nai, H. S. Shin, H. Y. Jeong, B. Liu, K. P. Loh, *Nat. Commun.* **2014**, *5*, 2995.

[31] A. Jawaid, D. Nepal, K. Park, M. Jespersen, A. Qualley, P. Mirau, L. F. Drummy, R. A. Vaia, *Chem. Mater.* **2015**, *28*, 337-348.

[32] T. H. Adam G. Kelly, Claudia Backes, Andrew Harvey, Amir Sajad Esmaeily, Ian Godwin, João Coelho, Valeria Nicolosi, Jannika Lauth, Aditya Kulkarni, Sachin Kinge, Laurens D. A. Siebbeles, Georg S. Duesberg, Jonathan N. Coleman, *Science* **2017**, *356*.

[33] D. Son, S. I. Chae, M. Kim, M. K. Choi, J. Yang, K. Park, V. S. Kale, J. H. Koo, C. Choi, M. Lee, J. H. Kim, T. Hyeon, D. H. Kim, *Adv. Mater.* **2016**, *28*, 9326-9332.

[34] D. J. P. de Sousa, L. V. de Castro, D. R. da Costa, J. M. Pereira, T. Low, *Phys. Rev. B* **2017**, *96*.

[35] A. Carvalho, M. Wang, X. Zhu, A. S. Rodin, H. Su, A. H. Castro Neto, *Nat. Rev. Mater.* **2016**, *1*.

[36] A. Castellanos-Gomez, L. Vicarelli, E. Prada, J. O. Island, K. L. Narasimha-Acharya, S. I. Blanter, D. J. Groenendijk, M. Buscema, G. A. Steele, J. V. Alvarez, H. W. Zandbergen, J. J. Palacios, H. S. J. van der Zant, *2D Mater.* **2014**, *1*, 025001.

[37] M. Köpf, N. Eckstein, D. Pfister, C. Grotz, I. Krüger, M. Greiwe, T. Hansen, H. Kohlmann, T. Nilges, *J. Cryst. Growth* **2014**, *405*, 6-10.

[38] G. Faraji, H. S. Kim, H. T. Kashi, *in Severe Plastic Deformation: Methods, Processing and Properties*, Armsterdam, Netherlands: Elsevier, **2018**.

[39] S. A. Ansari, M. S. Ansari, M. H. Cho, *Phys. Chem. Chem. Phys.* **2016**, *18*, 3921-3928.

[40] J. Kang, J. D. Wood, S. A. Wells, J. -H. Lee, X. Liu, K. -S. Chen, and M. C. Hersam, *ACS Nano* **2015**, *9*, 3596-3604.

[41] A. H. Woomer, T. W. Farnsworth, J. Hu, R. A. Wells, C. L. Donley, and S. C. Warren, *ACS Nano* **2015**, *9*, 8869-8884.

[42] D. Hanlon, C. Backes, E. Doherty, C. S. Cucinotta, N. C. Berner, C. Boland, K. Lee, A. Harvey, P. Lynch, Z. Gholamvand, S. Zhang, K. Wang, G. Moynihan, A. Pokle, Q. M. Ramasse, N. McEvoy, W. J. Blau, J. Wang, G. Abellan, F. Hauke, A. Hirsch, S. Sanvito, D. D. O'Regan, G. S. Duesberg, V. Nicolosi, J. N. Coleman, *Nat. Commun.* **2015**, *6*, 8563.

[43] S. H. Aldave, M. N. Yogeesh, W. Zhu, J. Kim, S. S. Sonde, A. P. Nayak, D. Akinwande, *2D Materials* **2016**, *3*, 014007.

[44] P. Avouris, *Nano Lett.* **2010**, *10*, 4285-4294.

[45] F. Bonaccorso, L. Colombo, G. Yu, M. Stoller, V. Tozzini, A. C. Ferrari, R. S. Ruoff, V. Pellegrini, *Science* **2015**, *347*, 1246501.

[46] A. K. Geim, K. S. Novoselov, *Nat. Mater.* **2007**, *6*, 183-191.

[47] X. Li, W. Cai, L. Colombo, and R. S. Ruoff, *Nano Lett.* **2009**, *9*, 4268-4272.

[48] S. H. Mir, L. A. Nagahara, T. Thundat, P. Mokarian-Tabari, H. Furukawa, A. Khosla, *J. Electrochem. Soc.* **2018**, *165*, B3137-B3156.

[49] K. Katagiri, *in Supra-materials Nanoarchitectonics (Eds.: K. Ariga, M. Aono)*, Elsevier, **2017**.

[50] L. Nicole, L. Rozes, C. Sanchez, *Adv. Mater.* **2010**, *22*, 3208-3214.

[51] D. J. Tranchemontagne, J. L. Mendoza-Cortes, M. O'Keeffe, O. M. Yaghi, *Chem. Soc. Rev.* **2009**, *38*, 1257-1283.

[52] M. Soler, G. R. Newkome, *Supramolecular Dendrimer Chemistry*, Wiley, **2012**.

[53] A. Gasparotto, D. Barreca, C. Maccato, E. Tondello, *Nanoscale* **2012**, *4*, 2813-2825.

[54] M. Tachibana, W. Engl, P. Panizza, H. Deleuze, S. Lecommandoux, H. Ushiki, R. Backov, Chem. Eng. Process.: Process Intensif. **2008**, *47*, 1317-1322.

[55] V. Maraval, J. Pyzowski, A. -M. Caminade, J. -P. Majoral, *J. Org. Chem.*

2003, *68*, 6043-6046.

[56] J. Jang, B. Lim, *Angew. Chem. Int. Ed.* **2003**, *42*, 5600-5603.

[57] H. Yoon, M. J. Choi, K. J. Lee, J. Jang, *Macromolecular Research* **2008**, *16*, 85-102.

[58] M. Winter,. R. J. Brodd, *Chem. Rev.* **2004**, *104*, 4245-4269.

[59] A. J. Bard, L. R. Faulkner, *Electrochemical methods: fundamentals and applications*, Weinheim: Wiley, **2001**.

[60] G. Z. Chen, *Int. Mater. Rev.* **2016**, *62*, 173-202.

[61] N. Kurra, R. Wang, H. N. Alshareef, *J. Mater. Chem. A* **2015**, *3*, 7368-7374.

[62] M. Kim, C. Lee, J. Jang, *Adv. Funct. Mater.* **2014**, *24*, 2489-2499.

[63] S. K. Kim, H. J. Koo, A. Lee, P. V. Braun, *Adv. Mater.* **2014**, *26*, 5108-5112.

[64] J. Oh, Y. K. Kim, J. S. Lee, J. Jang, *Nanoscale* **2019**, *11*, 6462-6470.

[65] S. Lee, Y. K. Kim, J. Y. Hong, J. Jang, *ACS Appl. Mater. Interfaces* **2016**, *8*, 24221-24229.

[66] N. A. Lanzillo, A. Glen Birdwell, M. Amani, F. J. Crowne, P. B. Shah, S. Najmaei, Z. Liu, P. M. Ajayan, J. Lou, M. Dubey, S. K. Nayak, T. P. O'Regan, *Appl. Phys. Lett.* **2013**, *103*, 093102.

[67] S. Yang, J. Kang, Q. Yue, K. Yao, *J. Phys. Chem. C* **2014**, *118*, 9203-9208.

[68] A. Splendiani, L. Sun, Y. Zhang, T. Li, J. Kim, C. Y. Chim, G. Galli, F. Wang, *Nano Lett.* **2010**, *10*, 1271-1275.

[69] N. Savjani, E. A. Lewis, R. A. D. Pattrick, S. J. Haigh, P. O'Brien, *RSC*

Adv. **2014**, *4*, 35609-35613.

[70] Y. Hou, L. Zhang, L. Y. Chen, P. Liu, A. Hirata, M. W. Chen, *Phys. Chem. Chem. Phys.* **2014**, *16*, 3523-3528.

[71] R. T. Gitti L. Frey, Manyalibo J. Matthews, M. S. Dresselhaus, G. Dresselhaus, *Phys. Rev. B* **1999**, *60*, 2883-2892.

[72] N. Su, H. B. Li, S. J. Yuan, S. P. Yi, E. Q. Yin, *eXPRESS Polym. Lett.* **2012**, *6*, 697-705.

[73] X. Zhao, Z. Zhao, M. Yang, H. Xia, T. Yu, X. Shen, *ACS Appl. Mater. Interfaces* **2017**, *9*, 2535-2540.

[74] T. M. L. Lawrence J. Willis, Kenneth F. Miller, Alice E. Bruce, and Edward I. Stiefel, *Inorg. Chem.* **1986**, *25*.

[75] Y. Huang, J. Ge, J. Hu, J. Zhang, J. Hao, Y. Wei, *Adv. Energy Mater.* **2018**, *8*, 1701601.

[76] P. L. Taberna, C. Portet, P. Simon, *Appl. Phys. A: Mater. Sci. Process.* **2005**, *82*, 639-646.

[77] K. Y. Shin, S. Lee, S. Hong, J. Jang, *ACS Appl. Mater. Interfaces* **2014**, *6*, 5531-5537.

[78] L. Kou, C. Chen, S. C. Smith, *J Phys. Chem. Lett.* **2015**, *6*, 2794-2805.

[79] T. Ramireddy, T. Xing, M. M. Rahman, Y. Chen, Q. Dutercq, D. Gunzelmann, A. M. Glushenkov, *J. Mater. Chem. A* **2015**, *3*, 5572-5584.

[80] B. V. S. a. F. G. J.S. LANNIN, *J. Non-Cryst. Solids* **1982**, *49*, 209-219.

[81] Z. Guo, H. Zhang, S. Lu, Z. Wang, S. Tang, J. Shao, Z. Sun, H. Xie, H. Wang, X.-F. Yu, P. K. Chu, *Adv. Funct. Mater.* **2015**, *25*, 6996-7002.

[82] H. B. Ribeiro, M. A. Pimenta, C. J. S. de Matos, *J. Raman Spectrosc.* **2018**, *49*, 76-90.

[83] L. Shao, H. Sun, L. Miao, X. Chen, M. Han, J. Sun, S. Liu, L. Li, F. Cheng, J. Chen, *J. Mater. Chem. A* **2018**, *6*, 2494-2499.

[84] J. Tabačiarová, M. Mičušík, P. Fedorko, M. Omastová, *Polym. Degrad. Stab.* **2015**, *120*, 392-401.

[85] E. R. Cordeiro, A. W. C. Fernandes, A. F. C. Pereira, M. M. d. Costa, M. L. F. Nascimento, H. P. d. Oliveira, *Quím. Nova* **2015**.

[86] A. Jorio, E. H. M. Ferreira, M. V. O. Moutinho, F. Stavale, C. A. Achete, R. B. Capaz, *Phys. Status Solidi B* **2010**, *247*, 2980-2982.

[87] M. M. Lucchese, F. Stavale, E. H. M. Ferreira, C. Vilani, M. V. O. Moutinho, R. B. Capaz, C. A. Achete, A. Jorio, *Carbon* **2010**, *48*, 1592-1597.

[88] J. Huang, *Electrochim. Acta* **2018**, *281*, 170-188.

[89] J. Jun, J. S. Lee, D. H. Shin, J. Oh, W. Kim, W. Na, J. Jang, *J. Mater. Chem. A* **2017**, *5*, 17335-17340.

[90] H. Yu, H. I. Yeom, J. W. Lee, K. Lee, D. Hwang, J. Yun, J. Ryu, J. Lee, S. Bae, S. K. Kim, J. Jang, *Adv. Mater.* **2018**, *30*.

[91] J. S. Lee, D. H. Shin, J. Jang, *Energy Environ. Sci.* **2015**, *8*, 3030-3039.

[92] M. H. Ryou, Y. M. Lee, J. K. Park, J. W. Choi, *Adv. Mater.* **2011**, *23*, 3066-3070.

[93] S. M. D. Haeshin Lee, William M. Miller, Phillip B. Messersmith, *Science* **2007**, *318*, 426-430.

[94] Z. Song, Y. Qian, X. Liu, T. Zhang, Y. Zhu, H. Yu, M. Otani, H. Zhou, *Energy Environ. Sci.* **2014**, *7*, 4077-4086.

[95] M. V. B. M. SAK-BOSNAR, S. KOVAC, S. KUKULJ, and L. DUIC, *J. Polym. Sci., Part A: Polym. Chem.* **1992**, *30*, 1609-1614.

[96] J. S. Park, A. Reina, R. Saito, J. Kong, G. Dresselhaus, M. S. Dresselhaus, *Carbon* **2009**, *47*, 1303-1310.

[97] L. G. Cancado, A. Jorio, E. H. Ferreira, F. Stavale, C. A. Achete, R. B. Capaz, M. V. Moutinho, A. Lombardo, T. S. Kulmala, A. C. Ferrari, *Nano Lett.* **2011**, *11*, 3190-3196.

[98] A. C. Ferrari, *Solid State Commun.* **2007**, *143*, 47-57.

[99] J. B. Wu, M. L. Lin, X. Cong, H. N. Liu, P. H. Tan, *Chem. Soc. Rev.* **2018**, *47*, 1822-1873.

[100] T. Liu, K. C. Kim, B. Lee, Z. Chen, S. Noda, S. S. Jang, S. W. Lee, *Energy Environ. Sci.* **2017**, *10*, 205-215.

[101] C. A. Matei Raicopol, Ruxandra Atasiei, Anamaria Hanganu, and Luisa Pilan, *J. Electrochem. Soc.* **2014**, *161*, G103-G113.

[102] A. Adhikari, S. Radhakrishnan, R. Patil, *Synth. Met.* **2009**, *159*, 1682-1688.

[103] S. J. Cooper, A. Bertei, D. P. Finegan, N. P. Brandon, *Electrochim. Acta* **2017**, *251*, 681-689.

[104] T. Q. N. a. C. Breitkopf, *J. Electrochem. Soc.* **2018**, *165*, E826-E831.

국문초록

수십 년 동안 많은 연구자들의 관심을 끌었던 나노 물질의 제조 및 심층 연구에 관한 수많은 연구가 진행되면서, 이와 더불어 유·무기 하이브리드 나노 물질의 제조에 대한 관심이 커지고 있다. 이러한 추세는 고성능과 안정성이 향상된 하이브리드 나노 재료를 사용하는 경량 에너지 저장 장치에 대한 IoT (Internet of Things) 시대의 수요를 따른다. 본 논문은 유기 및 무기 재료의 장점을 결합하여 에너지 저장 전자 장치에 적용함으로써 기능성 하이브리드 재료를 개발하는 데 중점을 두고 있다.

2차원 나노 물질은 십여 년 전의 획기적이었던 단층 그래핀 시트의 발견 이후 많은 관심을 끌고 있다. 그 후, 많은 2차원 무기 재료가 발견되고 연구되었으며, 이와 함께 유기 분자, 탄소 나노 튜브 및 폴리올레핀과 같은 다양한 탄소 재료가 유·무기 하이브리드 재료를 개발하기 위해 사용되어왔다. 하지만, 제조된 하이브리드 나노 물질 대부분은 2차원 재료의 전기화학적 거동이 억제된다는 단점이 있다.

따라서, 전도성 고분자는 전기화학적 특성을 유지하면서도

하이브리드 나노 재료로 조립될 때 기계적 및 열적 안정성을 향상시키는 훌륭한 후보이다. 가장 많이 연구된 전도성 고분자 중 하나인 폴리피롤(PPY)은 높은 전기 전도성, 전기화학적 활성 특성 및 환경 안정성을 고려하여 면밀히 조사되어 왔다. 그럼에도 불구하고, 2차원 나노 재료를 기판으로 이용하는 폴리피롤 기반 하이브리드 나노 물질의 구성은 여전히 도전 과제이다.

이 논문은 재료 설계 방법인 "통합 화학"을 기반으로, 구조화 반응을 통해 2차원 나노 기판을 조립하는 PPY 기반 하이브리드 나노 물질을 제작하는 세 가지 방법을 설명한다. MoS_2 나노 시트, 포스포린 및 도파민 코팅된 CVD-성장 그래핀은 빌딩 유닛으로서 사용되며, 구조화 반응동안 피롤 단량체와 조립된다. 본 연구에서는 통합 화학을 통해 3가지 종류의 PPY 기반 하이브리드 나노 재료를 슈퍼 커패시터 전극 재료로 활용하여 에너지 저장 성능은 물론 안정성이 우수한 것을 증명했다.

주요어: 하이브리드 나노재료; 통합 화학; 폴리피롤; MoS_2 나노시트; 포스포린; 그래핀; 슈퍼 커패시터
학 번: 2014-22591